This is a preprint, the final version is subject to change, of the American Mineralogist (MSA)
Cite as Authors (Year) Title. American Mineralogist, in press.
DOI: https://doi.org/10.2138/am-2019-6796

Textural and chemical variations of micas as indicators for tungsten mineralization: Evidence from highly evolved granites in the Dahutang tungsten deposit, South China

Revision 2

RONG YIN [a], LI HAN [a], XIAO-LONG HUANG [a,*], JIE LI [b], WU-XIAN LI [a], LIN-LI CHEN [a]

[a] State Key Laboratory of Isotope Geochemistry, Guangzhou Institute of Geochemistry, Chinese Academy of Sciences, Guangzhou 510640, China

[b] Key Laboratory of Submarine Geosciences, State Oceanic Administration; Second Institute of Oceanography, Ministry of Natural Resources, Hangzhou, 310012, China

[*] Corresponding author. Tel: +86-20-85290010.
E-mail address: xlhuang@gig.ac.cn (X.L. Huang)

ABSTRACT

The Dahutang tungsten deposit, located in the Yangtze Block, South China, is one of the largest tungsten deposits in the world. The tungsten mineralization is closely related to Mesozoic granitic plutons. A drill core through a pluton in the Dalingshang ore block in the Central segment of the Dahutang tungsten deposit shows that the pluton is characterized by multi-stage intrusive phases including biotite granite, muscovite granite, and Li-mica granite. The granites are strongly peraluminous and rich in P and F. Decreasing bulk-rock $(La/Yb)_N$ ratios and total rare earth element (∑REE) concentrations from the biotite granite to muscovite granite and Li-mica granite suggest an evolution involving the fractional crystallization of plagioclase. Bulk-rock Li, Rb, Cs, P, Sn, Nb and Ta contents increase with decreasing Zr/Hf and Nb/Ta ratios, denoting that the muscovite granite and Li-mica granite have experienced higher degree of magmatic fractionation than the biotite granite. In addition, the muscovite and Li-mica granites show M-type lanthanide tetrad effect, which indicates hydrothermal alteration during the post-magmatic stage. The micas are classified as lithian biotite and muscovite in the biotite granite, muscovite in the muscovite granite, and Li-muscovite and lepidolite in the Li-mica granite. The Li, F, Rb and Cs contents of micas increase, while FeO^T, MgO and TiO_2 contents decrease with increasing degree of magmatic fractionation. Micas in the muscovite granite and Li-mica granite exhibit compositional zonation in which Si, Rb, F, Fe and Li increase, and Al decreases gradually from core to mantle, consistent with magmatic differentiation. However, the outermost rim contains much lower contents of Si, Rb, F, Fe and Li, and higher Al than the mantle domains due to metasomatism in the presence of fluids. The variability in W contents of the micas matches the variability in Li, F, Rb and Cs contents, indicating that both the magmatic and hydrothermal evolutions were closely associated with W mineralization in the Dahutang deposit. The chemical zoning of muscovite and Li-micas not only traces the processes of W enrichment by magmatic differentiation and volatiles, but also the leaching of W by the fluids. Therefore, micas are indicators not only for the magmatic–hydrothermal evolution of granite, but also for the tungsten mineralization.

Keywords: mica, Dahutang tungsten deposit, highly evolved granite, magmatic evolution, hydrothermal evolution, South China

INTRODUCTION

Tungsten deposits are mainly involved in vein-like bodies, including quartz-greisen, quartz–sericite–K-feldspar, skarn, pegmatite, and quartz–tourmaline–chlorite rocks (Beus 1986), in which wolframite and scheelite are the two main tungsten-bearing ore minerals. Tungsten deposits are spatially and temporally associated with differentiated granites (Förster et al. 1999; Li et al. 2015; Lecumberri-Sanchez et al. 2017). The much higher partition coefficient of W in fluid than in granitic magma (Linnen and Cuney 2005) inhibits its mineralization in magma. Instead, W is leached by fluids and deposited in hydrothermal veins. It is therefore uncertain whether this spatial association implies a direct genetic link between tungsten mineralization and silicic magmatism, and how magmatic–hydrothermal processes contribute to tungsten mineralization (Hulsbosch et al. 2016). Whereas, the similar geochemical and isotopic features (including age) of both granites and vein-like W deposits might provide indirect evidence for a genetic link (Song et al. 2012; Huang and Jiang 2014; Zhang et al. 2017). The trace element and rare earth element (REE) compositions of scheelite and wolframite have been used to trace the source of W-bearing fluids (Song et al. 2014; Sun and Chen 2017; Harlaux et al. 2018; Zhang et al. 2018). However, the genetic source studies of tungsten cannot easily be constrained directly by investigation of ore veins alone. In addition, because differentiated intrusions are commonly concealed and unexposed, a direct genetic relationship with the ore deposit becomes difficult to establish.

Tungsten deposits are widely distributed globally, and China contains more than 60% of the world's tungsten reserves, which are particularly abundant in South China (Mao et al. 2013). The Dahutang tungsten deposit in South China has enormous resources estimated at up to two million tons of WO_3 (Huang and Jiang 2014). Quartz-vein-type wolframite associated with granite-related veinlets and disseminated scheelite are the dominant ore minerals in the Dahutang tungsten deposit (Huang and Jiang 2014; Jiang et al. 2015). Tungsten ore veins intrude Neoproterozoic biotite granodiorites and have a genetic link with buried late Mesozoic granites (Huang and Jiang 2014). Previous studies on the Dahutang tungsten deposit proposed that highly evolved granites in the late Mesozoic provided further enrichment of W in the magmatic intrusions (Mao et al. 2013, 2014; Huang and Jiang 2014). However, little is known about the mechanisms of W enrichment and its relationship to the magmatic and/or hydrothermal evolution. Indicator minerals in highly evolved granites may provide answers to these questions, in that they record the processes of both enrichment and transportation of tungsten. The chemical evolution and textural variation of micas have been suggested to trace the degree of differentiation and the magmatic–hydrothermal transition in highly evolved granite (Roda et al. 2007; Li et al. 2015; Breiter et al. 2017; Stepanov et al. 2014). Thus, micas may provide constraints on the mechanisms of W mineralization (Neiva 1987; Johan et al. 2012; Legros et al. 2016, 2018). In this paper, we present comprehensive in situ analyses of micas and whole-rock major and trace element compositions from drill cores through a granite in the Dalingshang ore block of Dahutang tungsten deposit. These data, together with the previously determined compositions of apatite and rutile (Han et al. 2015), offer an insight into the magmatic and hydrothermal evolution of the granitic pluton and the mechanisms of W mineralization, which can also provide the direct evidence of genetical link of tungsten deposit with the highly evolved granite.

GEOLOGICAL BACKGROUND, SAMPLES, AND PETROGRAPHY

The South China Block consists of the Yangtze Block in the northwest and the Cathaysia Block in the southeast (Fig. 1a). After amalgamation during the early Neoproterozoic, the two blocks experienced Caledonian, Indosinian, and Yanshanian tectono–magmatic activities (Li et al. 2002, 2008, 2009; Zhao et al. 2011). The extensive developments of rare metal mineralization are closely related to Mesozoic granitic magmatism (Mao et al. 2013). Mesozoic granitoid and volcanic rocks are widespread in the South China Block, and the large tungsten deposits (e.g., the Dajishan W deposit, the Xihuashan W deposit, and the Piaotang W–Sn deposit) are distributed mainly in the Nanling W–Sn polymetallic mineralization region (NLR; Fig. 1a), which is an area of significant economic rare metal mineralization in the Cathaysia Block (Zhao et al. 2017). Recently, large and super-large W deposits, such as Dahutang and Zhuxi deposits, have been discovered in the Yangtze Block (Huang and Jiang 2014; Song et al. 2018).

The Dahutang tungsten deposit is located near the southeastern margin of the Yangtze Block and the northern part of Jiuling Mountain in the center of the Jiangnan massif, part of the Qinhang belt (Mao et al. 2011) (Fig. 1a). Jiuling Mountain is a

Neoproterozoic granodiorite batholith intruding in the Shuangqiaoshan Group, which consists mainly of pelitic and psammitic metasedimentary rocks with metavolcanic horizons (Huang et al. 2003). The late Mesozoic granitic rocks, consisting of biotite granite, two-mica granite, muscovite granite, and granite porphyry, intruded mostly as stocks and veins into the Neoproterozoic granodiorite batholith and low-grade metamorphic rocks of the Shuangqiaoshan Group over multiple stages (Fig. 1b) (Lin et al. 2006; Huang and Jiang 2014; Mao et al. 2014). Late Mesozoic granitic stocks and veins are considered genetically related to the tungsten mineralization.

The Dahutang tungsten deposit includes the Shimensi ore block in the north segment, the Dalingshang ore block in the central segment, and the Shiweidong ore block in the south segment (Song et al. 2018a; Fig. 1b). The deposit is composed mainly of veinlets and disseminated orebodies, wolframite- and scheelite-bearing quartz veins, and W–Sn greisen (Jiang et al. 2015; Zhang et al. 2018). Jiang et al. (2015) and Song et al. (2018a) have summarized the published geochronological data of the Mesozoic granites from the Dahutang tungsten deposit and recognized two episodes of Mesozoic granitic magmatism (i.e., late Jurassic Period and early Cretaceous Period). The late Jurassic magmatism includes muscovite granite and biotite granite in the Shiweidong and Shimensi ore blocks, corresponding to LA-ICP-MS zircon U-Pb ages of 148–144 Ma (Jiang et al., 2015; Song et al. 2018b). The early Cretaceous intrusions consist of medium- to fine-grained two-mica granite, muscovite granite or granitic porphyry that occur in the Shiweidong and Dalingshang ore blocks, which have younger ages of 135–130 Ma (Jiang et al., 2015; Song et al.

2018b). The granitic porphyry, cutting through the granites and the orebodies, is considered as the latest intrusion (Lin et al. 2006; Song et al., 2018a).

The samples described in this study were all collected from core ZK15-1 that was drilled in the Dalingshang ore block, where Neoproterozoic biotite granodiorite is the host rock and was intruded by the late Mesozoic granites (Fig. 2) that are composed of biotite granite, muscovite granite and granite porphyry. The studied samples are predominantly biotite granite and muscovite granite with minor Li-mica granite (Fig. 3), and the detailed petrographic features of these rocks are provided below.

(i) Biotite granite

The biotite granite is porphyritic and consists predominantly of quartz (35%−40%), K-feldspar (34%−36%), plagioclase (18%−20%) and biotite (7%−10%) with minor muscovite (2%−4%). The phenocrysts include quartz (1−8 mm), K-feldspar (2−5 mm), and biotite (1−3 mm) in a groundmass of fine-grained plagioclase, quartz, biotite, and muscovite. Biotite grains contain abundant inclusions of zircon, apatite, ilmenite, and monazite (Figs. 3a, 3b and 3c), and some have been partially altered to chlorite. Muscovite always occurs at the margin of biotite or at the interfaces between other major rock-forming minerals (Fig. 3d).

(ii) Muscovite granite

The muscovite granite is medium- to fine-grained and contains quartz (20%−30%), K-feldspar (20%−30%), plagioclase (35%−45%) and muscovite (5%−15%). The muscovite occurs in two forms: coarse grains with irregular crystal boundaries that are euhedral to subhedral and 1–3 mm across, and fine grains that are several tens to hundreds of microns across and occur within feldspar as a result of sericitization (Fig. 3e). Accessory minerals include niobian rutile, cassiterite, pyrite, fergusonite-(Y), and apatite.

(iii) Li-mica granite

The Li-mica granite is porphyritic and represented by of quartz (25%−35%), K-feldspar (35%−45%), plagioclase (20%−25%) and Li-mica (5%−10%). The phenocrysts are represented by quartz (2−4 mm), K-feldspar (4−5 mm), plagioclase (1−3 mm), and Li-mica (1−2 mm). The larger Li-mica grains show irregular crystal boundaries (Fig. 3f). Fine-grained micas (300−800 μm) also occur in the interstices between other main minerals. Apatite, zircon, fluorite, and columbite-group minerals are common accessory minerals.

ANALYTICAL METHODS

Only fresh samples were selected for bulk-rock analysis. The rocks were crushed to <0.5 cm diameter, cleaned with deionized water in an ultrasonic bath, then dried and powdered in an agate mortar. The samples were prepared as glass disks using a Rigaku desktop fusion machine. Bulk-rock major element oxides were analyzed using a Rigaku RIX 2000 X-ray fluorescence spectrometer (XRF) at the State Key Laboratory of Isotope Geochemistry (SKLABIG), Guangzhou Institute of Geochemistry, Chinese Academy of Sciences (GIG-CAS). Calibration lines used in quantification were produced by bivariate regression of data from 36 reference

This is a preprint, the final version is subject to change, of the American Mineralogist (MSA)
Cite as Authors (Year) Title. American Mineralogist, in press.
DOI: https://doi.org/10.2138/am-2019-6796

materials encompassing a wide range of silicate compositions (Li et al. 2006). Calibrations incorporated matrix corrections based on the empirical Traill–Lachance procedure, and analytical uncertainties are mostly between 1% and 5% (Li et al. 2006). Additional determinations of F were performed by ALS Chemex (Guangzhou) Co Ltd, China, using the methods of KOH fusion and ion selective electrode, or Na_2O_2 fusion, citric acid leaching, and ion selective electrode transduction. F concentrations have <10% deviation from certified values. Trace elements were analyzed using inductively coupled plasma–mass spectrometry (ICP–MS) following acid digestion of samples (using a mixture of HF and HNO_3) in high-pressure Teflon vessels; details of the procedures are provided by Li et al. (2006). The USGS and Chinese National standards SARM-4, W-2, BHVO-2, AGV-2, GSR-1, GSR-2 and GSR-3 were chosen for calibrating the elemental concentrations of measured samples. Analytical precision for rare earth element (REE) and other incompatible element analyses is typically 1%–5%.

Polished thin sections were observed using a polarizing optical microscope and by scanning electron microscopy. The back-scattered-electron (BSE) images of micas and qualitative analysis of accessory minerals were obtained using field emission scanning electron microscopy (FESEM; Zeiss Supra55) or electron probe microanalysis (EPMA) using a JEOL JXA-8100 equipped with an Oxford Inca-X20 energy dispersive spectroscope (EDS) at the SKLABIG-GIG-CAS.

The major element compositions of micas were obtained by EPMA under the following conditions: 15 kV accelerating voltage, 20 nA beam current, 5 μm beam diameter, and a ZAF correction procedure for data reduction. The crystals used for the wavelength dispersive X-ray spectrometer (WDS) were TAP (for Si, Mg, Rb, Al, Na), LIF (for Fe, Mn, Ti), LDE1 (for F), and PETH (for K, Cs, Ca, P). A variable peak counting time of 7–60 s was used, depending on the intensity of the characteristic X-ray line and the desired precision. The detection limits for all elements were lower than 300 ppm. The following natural and synthetic standards were used: K-feldspar (for Si, K), pollucite (for Rb, Cs), apatite (for F, P), olivine (for Fe), Albite (for Na, Al), MnO (for Mn), kaersutite (for Ti), pyrope garnet (for Mg, Ca), and tugtupite (for Cl). Chemical formulae of micas were calculated based on 24 anions (O, F, OH), and Fe^{3+} was calculated following Lin and Peng (1994). The Li_2O content of micas was calculated following Tischendorf et al. (1997, 1999), and H_2O was calculated following Tindle and Webb (1990).

In situ trace element analyses of micas were obtained through laser ablation–inductively coupled plasma–mass spectrometry (LA–ICP–MS) using an Agilent 7500a ICP–MS coupled with a RESOlution M-50 laser ablation system at the SKLABIG-GIG-CAS. A spot size of 42 μm, a repetition rate of 5 Hz, and a maximum energy of 90 mJ were applied during analysis. External calibration used the National Institute of Standards NIST samples SRM 612 and T1-G with Al as the internal standards to correct for instrumental drift. Data reduction was performed using the commercial software ICPMSDataCal 6.7 (Liu et al. 2008). The detection limits of LA–ICP–MS range from 0.002 ppm for REE to 1 ppm for Ni. Repeat analyses of USGS rock standards SRM 612 and T1-G indicate that both precision and accuracy are better than 5% for most of the elements analyzed. For mica, the relative standard deviations (RSDs) of Rb, Cs, Nb, Ta, W and Sn are better than 1%; those of REE, Th, U and Pb range from 20% to 30%.

BULK-ROCK COMPOSITIONS

Nine granite samples (including three biotite granite, five muscovite granite and one lepidolite granite) from the Dalingshang ore block of the Dahutang tungsten deposit were analyzed for major and trace element compositions (Appendix 1). For comparison, we also collected data of two-mica granite from the Shiweidong ore block, as published by Huang and Jiang (2014).

Major elements

The analyzed rocks are strongly peraluminous (A/CNK = 1.25−1.42; Fig. 4a) with high SiO_2 (68.79−76.00 wt%), Al_2O_3 (12.8−17.2 wt%; Fig. 4b) and alkali (K_2O + Na_2O = 4.53−8.67 wt%) contents (Appendix 1). There is a general trend of decreasing TiO_2, MgO and Fe_2O_3 and from biotite granite to muscovite granite to Li-mica granite (Figs. 4c and 4d), and TiO_2 contents are positively correlated with MgO contents (Fig. 4c). The rocks are P- and F-rich granites with F contents of 0.28–1.65 wt% and P_2O_5 contents of 0.12–1.54 wt% (Appendix 1).

Trace elements

The studied samples contain relatively low REE contents (∑REE = 12−224 ppm). In chondrite-normalized REE patterns (Fig. 5a), they show strongly negative Eu anomalies (Eu/Eu^* = 0.02−0.47). The muscovite granite and Li-mica granite samples show the convex M-type lanthanide tetrad effect (Fig. 5a) with $TE_{1,3}$ values of 1.15−1.21 (Appendix 1). In addition, the ∑REE contents and Eu/Eu^* and $(La/Yb)_N$ values decrease gradually from biotite granite to muscovite granite to Li-mica granite (Appendix 1). In the mean upper crust normalized multi-elements diagram, the rocks are depleted in Ba, Sr, Ti, and REE, and enriched in Cs, Rb, W, Nb, Ta, P, Sn, and Li (Fig. 5b). Overall, the muscovite granite and Li-mica granite samples have much higher Li, Rb, Cs, P, W, Sn, Nb and Ta contents, and are depleted in Ba, Sr, Ti and REE relative to the biotite granite samples (Fig. 5b).

MICA CHEMISTRY

Micas in the biotite granite are compositionally homogeneous with abundant zircon, monazite, ilmenite and apatite inclusions (Figs. 3c and 3d). In contrast, micas in the muscovite granite and Li-mica granite exhibit compositional zoning that consists of core, mantle and rim domains (Fig. 6). The mantle domain is brighter than the core and rim domains in BSE images with a sharp compositional boundary between mantle and rim (Figs. 6b and 6d). The irregular rim is usually thin and may show a 'clinker'-like or porous morphology (Figs. 6b and 6d).

Major elements

Micas in studied samples show systematic chemical variability between different granite types. The micas in biotite granite samples consist of biotite and muscovite, which all have low Li_2O (0.17–1.10 wt%) and F (0.36–2.68 wt%) contents. The biotite has much higher FeO^T (18.7–25.0 wt%) and TiO_2 (1.53–3.18 wt%) contents and Fe/(Fe+Mg) and Fe^{2+}/Fe^{3+} ratios (0.58−0.78 and 9.17–13.51, respectively) than the muscovite (FeO^T = 1.40–4.35 wt%; TiO_2 = 0.23–1.02 wt%). Micas in muscovite granite and Li-mica granite samples show relatively high and variable Li_2O (0.21–2.59 wt% and 1.99–5.34 wt%, respectively) and F (0.07–7.87 wt% and 0.60–7.30 wt%, respectively) than the micas in biotite granite samples. They have low FeO^T (1.43–6.08 wt% and 0.02–5.43 wt%, respectively) and TiO_2 (≤0.72 wt% and ≤0.21 wt%, respectively) contents.

The micas in biotite granite samples are classified as lithian biotite (plotting between annite–phlogopite and zinnwaldite) and muscovite (Fig. 7). With increasing evolution from biotite granite to muscovite granite to Li-Mica granite, the micas show a trend of increasing Li content and decreasing Al and R^{2+} (where $R^{2+} = Fe^{2+} + Mn^{2+} + Mg^{2+}$) contents in the octahedral site (Fig. 7b). In the muscovite granite, the micas belong to muscovite with compositional changes toward zinnwaldite as increasing Li and Fe contents (Fig. 7). The micas in the Li-mica granite sample have higher Li but lower Fe contents than those in muscovite granite samples, which also show the compositional trend to trilithionite and polylithionite and are classified as Li-muscovite (0.5 trilithionite) or lepidolite (Fig. 7).

Overall, the Rb_2O contents of micas increase from biotite granite (≤0.46 wt%) through muscovite granite (0.11–1.43 wt%) to Li-mica granite (0.48–3.00 wt%). The micas also show a positive correlation between F and Rb_2O, and exhibit a trend of decreasing K/Rb ratio from biotite granite through muscovite granite to Li-mica granite (Figs. 8 and 9). Cesium is most enriched within trilithionite grains in the

Li-mica granite (up to 1.39 wt% Cs_2O) (Fig. 8). The Li, Rb and F contents of micas increase with decreasing K/Rb ratio from biotite granite through muscovite granite to Li-mica granite (Fig. 8).

Rare metal and other trace elements

Micas in studied samples have high and variable W, Sn, Nb and Ta contents (Fig. 9; Appendix 2), but contain extremely low REE contents, with most analyses being below the detection limits (bdl; Appendix 2). High K/Rb micas in biotite granite samples have relatively low W (1–99 ppm), Sn (15–273 ppm), Nb (21–151 ppm) and Ta (3–43 ppm) contents with variable Nb/Ta ratios (3.24−20.5) (Figs. 10a and 12; Appendix 2). Compared with the biotite granite, micas in the muscovite and Li-mica granites have higher Ta contents (10–182 ppm) and large variable Nb contents (9–261 ppm), which show overall lower Nb/Ta ratios (0.21–10.5) (Figs. 10a and 12; Appendix 2). Tungsten contents in micas increase from muscovite granite (7–140 ppm) to Li-mica granite (98–339 ppm), while Sn contents display a decreasing trend (89–737 ppm and 183–464 ppm, respectively). There is also an apparent decreasing trend in Sc contents from biotite granite (5.8–38.1 ppm) to muscovite granite (0.4–109 ppm) to Li-mica granite (0.3–0.8 ppm) (Appendix 2).

Compositional zoning

The zoned micas in muscovite granite samples have almost constant Si and Na contents and slightly decreasing Mg contents from core to mantle to rim (Fig. 11a). In contrast, the Fe, Rb and F contents increase gradually from core to mantle and then decrease in the rim. Aluminum contents decrease from core to mantle and increase in

DOI: https://doi.org/10.2138/am-2019-6796

rim (Fig. 11a). The mantle has higher Nb, Ta, W, Sn, Li and F contents than the core and rim (Fig. 12). The mean Nb/Ta ratio decreases gradually from core to mantle to rim (Fig. 12).

In zoned micas from Li-mica granite samples, the Si, Fe, Mn, Rb, Cs and F contents increase from core to mantle and show a notable decrease in rim, whereas Al contents decrease from core to mantle and then increase in rim (Fig. 11b). The core to mantle domains are characterized by compositions that change from Li-muscovite to lepidolite (Fig. 7); the rim domains are muscovite with relatively low Li and high Al contents (Fig. 7). The mantle domains have higher W, Ta, Li, Cs and F contents than the core and rim domains (Fig. 12). The Nb and Sn contents are higher in the core domains than in the mantle domains (Fig. 12). The Nb/Ta ratio also decreases from core (mean 7.68) to mantle (mean 0.54) to rim (mean 0.21) (Fig. 12).

DISCUSSION

Magmatic–hydrothermal evolution of the Dalingshang granite

Rare metal granites are considered to be highly fractionated bodies that record the transition between magmatic and hydrothermal processes (Cuney et al. 1992; Yin et al. 1995; Ballouard et al. 2016; Wu et al. 2017). The studied samples collected from ZK15-1 in the Dalingshang ore block of the Dahutang tungsten deposit are the late Mesozoic granites that intruded into the Neoproterozoic biotite granodiorite, and show a gradational variation in bulk-rock compositions from biotite granite through muscovite granite to Li-mica granite, which might reflect different degree of differentiation. The markedly negative Eu anomalies in bulk-rock composition (Fig. 5a) indicate extensive fractional crystallization of feldspars (plagioclase and K-feldspar). In addition, the gradual decrease in the $(La/Yb)_N$ ratio and ∑REE contents from biotite granite to muscovite granite and Li-mica granite (Appendix 1) are consistent with fractional crystallization of plagioclase, as the REEs are compatible in plagioclase in phosphorus-rich peraluminous felsic magmas with $D_{La} > D_{Yb}$ (Bea et al. 1994). The fractionation of K-feldspar and plagioclase in highly evolved granites also depletes the melt in Ba and Sr, respectively (Nash and Crecraft 1985; Bea et al. 1994), corresponding to negative Ba and Sr anomalies in studied samples (Fig. 5b). The depletion in Ti is likely caused by the fractional crystallization of Fe–Ti oxides, in particular rutile and ilmenite.

Plagioclase feldspar preferentially incorporates Sr over Rb (Nash and Crecraft 1985; Bea et al. 1994), zircon partitions Zr over Hf (Linnen and Keppler 2002; Yin et al. 2013), and micas and columbite-group minerals preferentially incorporate Nb over Ta (Linnen and Keppler 1997; Stepanov et al. 2014). In addition, Rb would be enriched in the residual melt, whereas K is almost invariable. Therefore, K/Rb, Zr/Hf, Nb/Ta and Rb/Sr ratios are useful indicators of the degree of differentiation of magmas (Bau 1996; Dostal and Chatterjee 2000; Deering and Bachmann 2010; Ballouard et al. 2016). The studied samples show increasing Rb/Sr ratio and decreasing Zr/Hf, Nb/Ta and K/Rb ratios from biotite granite to muscovite granite and Li-mica granite (Appendix 1), indicating the elevated degree of differentiation.

Whole-rock Nb/Ta ratios of <5 has been regarded as geochemical marker of highly evolved melt with hydrothermal interaction (Ballouard et al. 2016). Both the muscovite granite and Li-mica granite samples have very low Nb/Ta ratios (0.94–3.19; Appendix 1), suggesting a magmatic-hydrothermal evolution. In their REE patterns, the muscovite granite and Li-mica granite samples show convex M-type lanthanide tetrad effect ($TE_{1,3}$ > 1.1; Fig. 5a, Appendix 1) similar to many highly evolved granites related to W-Sn deposit (e.g., Zhao et al. 1992; Monecke et al. 2007). In general, the lanthanide tetrad effect is due to different partition coefficients of REE–F and REE–Cl complexes in the fluid phase (Bau 1996; Irber 1999; Monecke et al. 2011). The F-rich hydrosaline magmatic fluid-melt interaction might enhance the M-type lanthanide tetrad effect in the silicate melt (Wu et al. 2011; Peretyazhko and Savina 2010). In addition, fluid-melt interaction in an open system may produce M-type lanthanide tetrad effect because of the remove of coexisting or exsolved fluids that show complementary W-type REE pattern (Irber 1999). As a result, both the rock-forming minerals and accessory minerals can also show M-type lanthanide tetrad effect (Monecke et al. 2002; Wu et al. 2011). Therefore, we proposed that the M-type lanthanide tetrad effect recorded in studied samples reflects interaction with hydrothermal fluids during the post-magmatic stage. However, crystallization of niobian rutile, cassiterite, and fergusonite-(Y) in the muscovite granite and columbite-group minerals in the Li-mica granite represent the saturation of rare metal elements in the melt.

The evolutionary trend of the magma and the degree of fractionation inferred from mica compositions are comparable to those deduced from zircon and columbite-group minerals in rare metal granites (van Lichtervelde et al. 2008; Stepanov et al. 2014; Li et al. 2015; Breiter et al. 2017). In rare metal granites, volatile elements (e.g., F and P) and incompatible elements (e.g., Li, Rb, Cs) are gradually enriched as the magma evolves and fractionates to become saturated during the post-magmatic stage (Huang et al. 2002; Wu et al. 2017). In the granites of the Dalingshang ore block, the differentiation of the granitic plutons means that the Li, Rb and F contents in the micas increase in proportion to their concentrations in the magma (Fig. 8). The crystallization of Li-mica in the muscovite and Li-mica granite is an important mineralogical marker of the saturation of volatile elements during the post-magmatic stage. A trend of increasing fractionation is also indicated by the decreasing Nb/Ta ratios recorded in the micas, according to the higher compatibility of Nb over Ta in micas in granite magmas (Stepanov et al. 2014). The FeO^T, MgO and TiO_2 contents and Nb/Ta and K/Rb ratios in micas all decrease from biotite granite to muscovite granite to Li-mica granite (Figs. 9, 10), consistent with a fractional crystallization trend. The K/Rb and Nb/Ta ratios in micas from studied samples (3.1–73 and 0.21–21, respectively) are higher than those within the Yashan granite (1.67–41 and 0.26–7, respectively; Li et al. 2015) that hosts a Ta deposit in South China, thereby indicating a lower degree of fractionation than the Yashan granite.

The micas in the muscovite granite and the Li-mica granite show distinctive patterns of zoning (Fig. 6), suggesting a change in the composition of the melt, which may record differentiation, magma mixing, or fluid metasomatism (e.g., Vernon et al. 1988; Clarke et al. 2003; Roda et al. 2007; Li et al. 2013). For compositional zoned mica, the core would crystallize from original magma. The F, Li, Fe, Rb and Cs contents in zoned muscovite-lepidolite of studied samples increase gradually from core to mantle, which lead to different brightness of zoning texture in BSE (Fig. 6), consistent with the trend of magmatic evolution (e.g., Roda et al. 2007). Given the high partition coefficient of Cs in fluids (Webster et al. 1989), the distinct enrichment of Cs in the mantle domains of zoned micas suggests interaction with hydrothermal fluids that may have exsolved from the granitic magma as it differentiated (Černý et al. 1985; Wang et al. 2004). The irregular rims, which are characterized by a porous 'clinker-like' structure, possibly indicate later metasomatism of relict mantles (Fig. 6d). As the rim domains contain very low Li, F, Rb and Cs contents relative to the core and mantle domains (Fig. 11), we propose that an exotic aqueous fluid was involved in the magmatic–hydrothermal evolution (see in following section).

Tungsten enrichment during magmatic evolution

Rare metal granites are an important host of W–Sn–Nb–Ta polymetallic deposits (Černý et al. 2005). These rare metals have a similar ionic radius and electronegativity, and show similar geochemical characteristics (Linnen and Cuney 2005). However, they exhibit different geochemical behaviors during mineralization according to slight differences in solubility and fluid–melt partition coefficients (Linnen 1998; Linnen and Cuney 2005). Columbite-group minerals, ixiolite and microlite are homogeneously disseminated within the granites, consistent with a magmatic origin for Nb and Ta mineralization. The volatile elements, especially Li and F, promote Ta crystallization and Nb–Ta differentiation (Linnen 1998; van Lichtervelde et al. 2008).

Sn is disseminated in granites or closely related to hydrothermal processes, including the formation of greisen, skarns, and felsic veins (Lehmann 1987; Pollard et al. 1987; Bhalla et al. 2005). Tungsten is mainly deposited in hydrothermal veins (Lecumberri-Sanchez et al. 2017). The three types of ore-bearing granites exhibit different evolutionary trends, in which W or W–Sn mineralization is closely related to biotite granites, two-mica granites or muscovite granites, and Nb–Ta deposits mostly relate to albite granites that record a higher degree of differentiation (Chen et al. 2008; Huang et al. 2002; Li et al. 2015; Wang et al. 2017).

Tungsten is incompatible in granitic melt and is consequently enriched in highly evolved granites that are aluminous and volatile-enriched. For example, the Erzgebirge granites exhibits increasing W contents from low-F biotite granite through low-F two-mica granite to high-F and high-P Li-mica granite (Förster et al. 1999). Experimental studies show that W exists mainly as the W^{6+} ion and constitutes WO_4^{2-} tetrahedra within the granitic melt (Farges et al. 2006). Because of the different geometric properties and larger volume of [WO_4] relative to [SiO_4], [WO_4] is not readily incorporated into the crystal lattice of rock-forming minerals. Therefore, tungsten becomes enriched in the residual melt during differentiation due to the fractional crystallization of plagioclase. Alkali metals such as Na and K are available to interact with WO_4^{2-} tetrahedra to promote W solubility (Linnen and Cuney 2005). Tungsten is likely to become saturated in aluminous granites because of the lower solubility of wolframite in aluminous melt compared with alkali melt (Che et al. 2013). The fluorine input may increase the abundance of NBOs (non-bridging oxygens) (Mysen 1990; Keppler 1993), which may increase the proportion of WO_4^{2-} tetrahedral in the melt (Che et al. 2013). Therefore, tungsten will become enriched in the melt of the post-magmatic stage, when the melt is highly fractionated and depolymerized.

Granites in the Dalingshang ore block are peraluminous and highly evolved. The muscovite granite and Li-mica granite have lower K/Rb ratios than the biotite granite and show lanthanide tetrad effect, consistent with the magmatic–hydrothermal stage. The muscovite granites have slightly higher W contents than the biotite granite and Li-mica granite (Fig. 10f), whereas muscovite and Li-mica (Li-muscovite and lepidolite) show much higher W contents than biotite grains (Fig. 10c). This indicates that the precipitation of W has a close affinity with mica growth, in particular muscovite and Li-mica. The ionic radius of W^{6+} (0.68 Å) is close to that of Ti^{4+} (0.69 Å), and tungsten is able to enter octahedral vacancies such as occur in rutile and biotite (Shannon 1976). Thus, during the early magmatic stage of the Dalingshang granite, biotite and rutile were the major carriers of W. Because of the similar ionic radii and electronegativity of W^{6+} (0.68 Å, 984 kJ/mol) and Al^{3+} (0.61 Å, 921 kJ/mol) (Shannon 1976), W^{6+} can replace tetrahedral Al^{3+} in muscovite. The trace element contents of micas are also dependent on the partition coefficient of W between micas and melts, although few data exist. Antipin et al. (1981) reported that W is compatible within micas. Simons et al. (2017), in a study of peraluminous granites of the Cornubian Batholith in Europe, showed that micas are major rock-forming minerals containing W, in which muscovite and Li-micas have higher W contents than biotite.

Muscovite has a much higher D_W value than biotite with calculation (Simons et al. 2017). Therefore, muscovite and Li-mica are effective carriers of tungsten, which resulted in the muscovite granite and Li-mica granite in the Dahutang tungsten deposit being enriched in W.

The zoned micas in the muscovite and Li-mica granites in the Dalingshang ore block could be utilized to investigate magmatic–hydrothermal processes through variations in the concentrations of trace elements such as Li, F, Rb and Cs. Enrichment in Ta and W is greater in the mantle domain of zoned micas and shows positive correlations with Li, F, Rb and Cs contents (Fig. 12). In contrast, Nb and Sn contents decrease from core to mantle (Fig. 12), which may record the crystallization of other accessory minerals, such as columbite-group minerals, or may indicate the role of fluid-related alteration. Both W and Ta contents in micas are strongly correlated with Li, F, Rb and Cs contents, suggesting that enrichment of W and Ta is associated with magmatic evolution and has a close affinity with Li and F (Fig. 12).

Effect of fluid on W mineralization

The predominant occurrences of scheelite and wolframite are dip-dying veinlet-type and quartz-vein-type, respectively, rather than magmatic type, which suggests that a tungsten deposit is unlikely to form in magma although magmatic evolution may result in enrichment in W (Beus 1986; Lecumberri-Sanchez et al. 2017). Tungsten is different from other rare metals that are commonly enriched in magmatic–hydrothermal ore deposits as it is transported mainly as anionic species such as $NaWO_4^-$, HWO_4^-, and WO_4^{2-} within mineralizing fluids (Wood and Samson

2000; Zajacz et al. 2008). Consequently, tungsten can be transported long distances via aqueous fluids. The selective crystallization of wolframite or scheelite from aqueous fluids is controlled by different cationic species (Fe^{2+}, Mn^{2+} or Ca^{2+}) under suitable physicochemical conditions (Wood and Samson 2000).

The zoned micas in the muscovite and Li-mica granite from the Dalingshang ore block of the Dahutang tungsten deposit trace not only the enrichment but also the leaching process of rare metal elements. Most high field strength elements (i.e., W, Sn and Nb) in the rim domains have concentrations that are distinctly lower than in the core and mantle domains (Figs. 12e, 12f and 12g), which may reflect the alteration in the presence of fluids. Fluid cannot effectively transport Nb and Ta due to extremely low fluid–melt partition coefficients (Linnen and Cuney 2005). However, as the Nb/Ta ratios are lowest in the rim domains of zoned micas, we suggest that Nb is more easily taken away than Ta in fluid. The partition coefficient for W between melt and fluid varies greatly from 0.37 to 4.1 (Keppler and Wyllite 1991), due to the combined effect of the chlorine content of the fluid, pH value, and oxygen fugacity (Zajacz et al. 2008). The $D_W^{fluid/melt}$ value is lower in high-HCl or high-HF aqueous solutions (Kepple and Wyllite 1991). Manning and Henderson (1984) reported a positive correlation between $D_W^{fluid/melt}$ and the NaCl and NaF contents of the fluid, whereas Bai and van Groos (1991) noted a decrease in $D_W^{fluid/melt}$ with the addition of NaCl. Therefore, the decrease of W in the rim of zoned Li-micas reflects the extraction of W by a fluid. In addition, bulk-rock Nb and Ta contents increase gradually from biotite granite to muscovite granite to Li-mica granite (Fig. 10), which differs from the trend in W, further demonstrating that hydrothermal fluids played an important role in W mineralization (Li et al. 2015).

Based on the occurrence and compositions of apatite and rutile in granites of Dalingshang ore block, a late hydrothermal stage is inferred, in which oxygen fugacity is significantly low and corresponds to a relatively reducing environment (Han et al. 2015). Under such conditions, Mn and Fe mainly exist in a divalent state, enabling complexing with WO_4^{2-} to form wolframite ($[Fe,Mn]WO_4$). In addition, Ca^{2+} derived from hornblende and plagioclase due to fluid-mediated wall-rock alteration (Jiang et al. 2015) may combine with WO_4^{2-} to form scheelite ($CaWO_4$). A detailed fluid-inclusion study reported that ore-forming fluids in the Dahutang tungsten deposit were of low salinity and low to moderate temperature (Gong et al. 2013). The homogenization temperatures of the fluid inclusions in the Shimensi ore block are mainly 200–270°C and the salinity (NaCl equiv.) is in the range 0.18–9.47 wt % (Gong et al. 2013). Wang et al. (2015) studied the composition of sulfur isotopes in the Dahutang tungsten deposit and showed that $\delta^{34}S$ values of chalcopyrite and molybdenite show slight variation (–3.1‰ to 0.9‰) and have the characteristics of magmatic sulfur. In addition, hydrogen and oxygen isotopic data from ore-bearing quartz in the Dahutang tungsten deposit ($\delta D_{V\text{-}SMOW}$ = -76‰ to -64‰; $\delta^{18}O_{H2O}$ = 4.5‰ to 7.3‰) plot in the field of magmatic water in the δD vs. $\delta^{18}O_{H2O}$ diagram, with a small component of meteoric water (Wang et al. 2015).

IMPLICATIONS FOR W MINERALIZATION

The crystallization and differentiation of granitic magma lead to an enrichment in incompatible elements and play an important role in rare metal mineralization (Förster et al. 1999; Huang et al. 2002; Linnen and Cuney 2005). The process is also accompanied with the magmatic-hydrothermal evolution and the saturation of volatile elements. The granites of the Dalingshang ore block are highly evolved, which have been inferred to be the parent rocks of the Dahutang tungsten deposit (Huang and Jiang 2014) and may have undergone multiple stages of mineralization (Song et al. 2018b). However, little is known of magmatic–hydrothermal processes that influenced the behavior of rare metal enrichment in the granites. Based on the chemical evolution and textural variation of micas in the Dalingshang granites, we proposed the ore-forming processes in the Dahutang tungsten deposit as shown in the schematic diagram (Fig. 13) and discussed below.

(1) The magmatic evolution is from biotite granite to muscovite granite to Li-mica granite. The biotite granite represents the early magmatic stage. The highly evolved muscovite granite and Li-mica granite were formed from hydrous and low-viscosity magmas in a magma and hydrothermal fluid coexisting environment, which represent the post-magmatic stage. The ore-forming elements and volatiles became saturated during the post-magmatic stage.

(2) Micas are effective indicator not only for the magmatic-hydrothermal evolution of the granite, but also for the tungsten mineralization process. The

enrichment of W has the affinity with volatiles. When the residual melts interact with internally or externally derived fluid, this fluid can extract rare metals in the melts and micas and form a low tungsten rim in zoned muscovite.

(3) Tungsten can be taken away distantly by the fluid (Lecumberri-Sanchez et al. 2017). The ore-forming elements, in particular tungsten, are unlikely to be deposited directly in the granite, and reducing fluids and fluid–rock interaction play an import role in forming large ore deposits.

Tungsten mineralization is always related to highly evolved S-type granites (Förster et al. 1999; Zhao et al. 2017; Zhang et al. 2017). In Dahutang tungsten deposit, the textural and componential variations of micas could be utilized as an optimal proxy to judge the parent rocks of W deposit and estimate the W metallogenic potential of the granites. In this study, enrichment in W is closely related to crystallization of muscovite and Li-mica (Li-muscovite and lepidolite) during the post-magmatic stage. The rims of zoned muscovite record the interaction by fluids, which is a universal feature of tungsten-bearing granites and veins (Li et al. 2013, 2015, 2018; Legros et al. 2016, 2018). Thus, muscovite and Li-micas are indicator minerals for tungsten ore-forming potential in the granites. It is a common feature that the micas of the tungsten granites, such as the Xihuashan granites in South China (Li et al. 2013), Yashan rare-metal granite (Li et al. 2015), and the Erzgebirge granites in Germany (Breiter et al. 2017), all exhibit large extent of compositional variation or variable compositional zoning, which would be important for reconstructing tungsten ore-forming process. The textural of zoned micas and geochemical variations of micas in these tungsten granites may also record the processes of both enrichment and transportation of tungsten during the magmatic-hydrothermal evolution.

ACKNOWLEDGMENTS

We appreciate Q.S. Zuo and G.L. Zhan for fieldworks, Y. Liu, C.Y. Li, and X.L. Tu for analytical assistance. We acknowledge the constructive comments of two anonymous reviewers, which helped considerably in improving the manuscript. This study was financially supported by the National Key Research and Development Program of China (No. 2016YFC0600204) and National Natural Science Foundation of China (NSFC Projects 41602035, 41625007, U1701641). This is contribution No. IS-XXXX from GIG-CAS.

REFERENCES

Antipin, V.S., Kovalenko, V.I., Kuznetsova, A.I., and Persikova, L.A. (1981) Tin and tungsten behavior in ore-bearing acidic magmatic rocks according to analyses of the partition coefficients. Geokhimiya, 2, 163–177.

Bai, T.B., and van Groos, A.F.K. (1999) The distribution of Na, K, Rb, Sr, Al, Ge, Cu, W, Mo, La, and Ce between granitic melts and coexisting aqueous fluids. Geochimica et Cosmochimica Acta, 63, 1117–1131.

Ballouard, C., Marc Poujol, M., Boulvais, P., Branquet, Y., Tartèse, R., and Vigneresse, J. (2016) Nb–Ta fractionation in peraluminous granites: a marker of the magmatic-hydrothermal transition. Geology, 44, 231–234.

Bau, M. (1996) Controls on the fractionation of isovalent trace elements in magmatic and aqueous systems: evidence from Y/Ho, Zr/Hf, and lanthanide tetrad effect. Contributions to Mineralogy and Petrology, 123, 323–333.

Bea, F., Pereira, M.D., and Stroh, A. (1994) Mineral/leucosome trace-element partitioning in a peraluminous migmatite (a laser ablation-ICP-MS study). Chemical Geology, 117, 291–312.

Beus, A.A. (1986) Geology of tungsten. International Geological Correlation Programme, Project 26 Mawam, pp. 59–65.

Bhalla, P., Holz, F., Linnen, R.L., Behrens, H. (2005) Solubility of cassiterite in evolved granitic melts: effect of T, fO_2, and additional volatiles. Lithos, 80, 387–400.

Breiter, K., Vankova, M., Galiova, M.V., Korbelova, Z., and Kanicky, V. (2017) Lithium and trace-element concentrations in trioctahedral micas from granites of different geochemical types measured via laser ablation ICP-MS. Mineralogical Magazine, 81, 15–33.

Černý, P., Meintzer, R.E., and Anderson, A.J. (1985) Extreme fractionation in rare-element granitic pegmatites: selected examples of data and mechanisms. Canadian Mineralogist, 23, 381–421.

Černý, P., Blevin, P.L., Cuney, M., and London, D. (2005) Granite-related deposits. Economic Geology 100th Anniversary Volume, Society of Economic Geologists, 337–370.

Chen, J., Lu, J.J., Chen, W.F., Wang, R.C., Ma, D.S., Zhu, J.C., Zhang, W.L., and Ji, J.F. (2008) W-Sn-Nb-Ta-bearing granites in the Nanling Range and their relationship to metallogenesis. Geological Journal of China Universities, 14, 459–473 (in Chinese with English abstract).

Che, X.D., Linnen, R.L., Wang, R.C., Aseri, A., and Thibault, Y. (2013) Tungsten solubility in evolved granitic melts: An evaluation of magmatic wolframite: Geochimica et Cosmochimica Acta, 106, 84–98.

Clarke, D.B., and Bogutyn, P.A. (2003) Oscillatory epitactic-growth zoning in biotite and muscovite from the Lake Lewis leucogranite, South Mountain Batholith, Nova Scotia, Canada. Canadian Mineralogist, 41, 1027–1047.

Cuney, M., Marignac, C., and Weisbrod, A. (1992) The Beauvoir topaz-lepidolite albite granite (Massif Central, France); the disseminated magmatic Sn-Li-Ta-Nb-Be mineralization. Economic Geology, 87, 1766–1794.

Deering, C.D., and Bachmann, O. (2010) Trace element indicators of crystal accumulation in silicic igneous rocks. Earth and Planetary Science Letters, 297, 324–331.

Dostal, J., and Chatterjee, A.K. (2000) Contrasting behaviour of Nb/Ta and Zr/Hf ratios in a peraluminous granitic pluton (Nova Scotia, Canada). Chemical Geology, 163, 207–218.

Farges, F., Linnen, R.L., and Brown, G.E. (2006) Redox and speciation of tin in hydrous silicate glasses: a comparison with Nb, Ta, Mo and W. Canadian Mineralogist, 44, 795–810.

Förster, H.J., Tischendorf, G., Trumbull R.B., and Gottesmann, B. (1999) Late-collisional granites in the Variscan Erzgebirge, Germany. Journal of Petrology, 40, 1613–1645.

Foster, M.D. (1960) Interpretation of the composition of trioctahedral micas. U.S. Geological Survey Professional Paper, 354-E, 115–147.

Gong, X.D., Zhang, Z.H., Yao, X.F., He, P., Li, Y.P., Zhen, S.M., 2013. A brief analysis of the ore-forming fluid in Dahutang tungsten deposit in Wuning, Jiangxi Province. Acta Mineralogica Sinica, S2 (suppl.), 445–446 (in Chinese).

Han, L., Huang, X.L., Li, J., He, P.L., and Yao, J.M. (2015) Oxygen fugacity variation recorded in apatite of the granite in the Dahutang tungsten deposit, Jiangxi Province, South China. Acta Petrologica Sinica, 32, 746–758 (in Chinese with English abstract).

Harlaux, M., Mercadier, J., Marignac, C., Peiffert, C., Cloquet, C., Cuney, M. (2018) Tracing metal sources in peribatholitic hydrothermal W deposits based on the chemical composition of wolframite: The example of the Variscan French Massif Central. Chemical Geology, 479, 58–85.

Huang, L.C., and Jiang, S.Y. (2014) Highly fractionated S-type granites from the giant Dahutang tungsten deposit in Jiangnan Orogen, Southeast China: Geochronology, petrogenesis and their relationship with W mineralization. Lithos, 202, 207–226.

Huang, X., Yu, Z., and Zhou, G. (2003) Sedimentary features of the Mesoproterozoic Shuangqiaoshan Group in northwestern Jiangxi. Geological Bulletin of China, 22, 43–49 (in Chinese with English abstract).

Huang, X.L., Wang, R.C., Chen, X.M., Hu, H., and Liu, C.S. (2002) Vertical variations in the mineralogy of the Yichun topaz-lepidolite granite, Jiangxi Province, southern China. Canadian Mineralogist, 40, 1047–1068.

Hulsbosch, N., Boiron, M.C., Dewaele, S., and Muchez, P. (2016) Fluid fractionation of tungsten during granite–pegmatite differentiation and the metal source of peribatholitic W quartz veins: Evidence from the Karagwe-Ankole Belt (Rwanda). Geochimica et Cosmochimica Acta, 175, 299–318.

Irber, W. (1999) The lanthanide tetrad effect and its correlation with K/Rb, Eu/Eu*, Sr/Eu, Y/Ho, and Zr/Hf of evolving peraluminous granite suites. Geochimica et Cosmochimica Acta, 63, 489–508.

Jiang, S.Y., Peng, N.J., Huang, L.C., Xu, Y.M., Zhan, G.L., and Dan, X.H. (2015) Geological characteristic and ore genesis of the giant tungsten deposits from the

Dahutang ore-concentrated district in northern Jiangxi Province. Acta Petrologica Sinica, 31, 639–655 (in Chinese with English abstract).

Johan, Z., Strnad, L., and Johan, V. (2012) Evolution of the Cínovec (zinnwald) granite cupola, Czech Republic: composition of feldspars and micas, a clue to the origin of W, Sn mineralization. Canadian Mineralogist. 50, 1131–1148.

Keppler, H. (1993) Influence of fluorine on the enrichment of high field strength trace elements in granitic rocks. Contributions to Mineralogy and Petrology, 114, 479–488.

Keppler, H., and Wyllie, P. J. (1991) Partitioning of Cu, Sn, Mo, W, U, and Th between melt and aqueous fluid in the systems haplogranite-H_2O–HCl and haplogranite-H_2O–HF. Contributions to Mineralogy and Petrology, 109, 139–150.

Lecumberri-Sanchez, P., Vieira, R., Heinrich, C.A., Pinto, F., and Walle, M. (2017) Fluid-rock interaction is decisive for the formation of tungsten deposits. Geology, 45, 579–582.

Legros, H., Marignac, C., Mercadier, J., Cuney, M., Richard, A., Wnag, R.C., Charles. N., and Lespinasse, M.Y. (2016) Detailed paragenesis and Li-mica compositions as recorders of the magmatic-hydrothermal evolution of the Maoping W-Sn deposit (Jiangxi, China). Lithos, 264, 108–124.

Legros, H., Marignac, C., Tababy, T., Mercadier, J. Richard, A., Cuney, M., Wang, R.C., Charles., N., and Lespinasse, M.Y. (2018) The ore-forming magmatic-hydrothermal system of the Piaotang W-Sn deposit (Jiangxi, China) as seen from Li-mica geochemistry. American Mineralogist, 103, 39–54.

Lehmann B. (1987) Tin granites, geochemical heritage, magmatic differentiation. Geologische Rundschau, 76, 177–185.

Li, J., Huang, X.L., Wei, G.J., Liu, Y., Ma, J.L., Han, L., He, P.L. (2018) Lithium isotope fractionation during magmatic differentiation and hydrothermal processes in rare-metal granites. Geochimica et Cosmochimica Acta, 240, 64–79.

Li, J., Huang, X.L., He, P.L., Li, W.X., Yu, Y., Chen, L.L. (2015) In situ analyses of micas in the Yashan granite, South China: constraints on magmatic and hydrothermal evolutions of W and Ta-Nb bearing granites. Ore Geology Reviews, 65, 793–810.

Li, J., Zhong, J.W., Yu, Y., Huang, X.L., (2013) Insights on magmatism and mineralization from micas in the Xihuashan granite, Jiangxi Province, South China. Geochimica, 42, 393–404 (in Chinese with English abstract).

Li, W.X., Li, X.H., Li, Z.X., and Lou, F.S. (2008) Obduction-type granites within the NE Jiangxi Ophiolite: implications for the final amalgamation between the Yangtze and Cathaysia Blocks. Gondwana Research, 13, 288–301.

Li, X.H., Li, W.X., Li, Z.X., Lo, C.H., Wang, J., Ye, M.F., and Yang, Y.H. (2009) Amalgamation between the Yangtze and Cathaysia Blocks in South China: constraints from SHRIMP U-Pb zircon ages, geochemistry and Nd-Hf isotopes of the Shuangxiwu volcanic rocks. Precambrian Research, 174, 117–128.

Li, X.H., Li, Z.X., Wingate, M.T.D., Chung, S.L., Liu, Y., Lin, G.C., and Li, W.X. (2006) Geochemistry of the 755 Ma Mundine Well dyke swarm, northwestern Australia: part of a Neoproterozoic mantle superplume beneath Rodinia? Precambrian Research, 146, 1–15.

Li, Z.X., Li, X.H., Zhou, H.W., and Kinny, P.D. (2002) Grenvillian continental collision in south China: new SHRIMP U-Pb zircon results and implications for the configuration of Rodinia. Geology, 30, 163–166.

Li, Z.X., Li, X.H., Wartho, J.A., Clark, C., Li,W.X., Zhang, C.L., and Bao, C.M. (2010) Magmatic and metamorphic events during the early Paleozoic Wuyi-Yunkai orogeny, southeastern South China: new age constraints and pressure–temperature conditions. Geological Society of America Bulletin, 122, 772–793.

Lin, L., Zhan, G.L., Yu, X.P. (2006) The metallogenic prognosis of Dahutang tungsten ore field in Jiangxi. Resources Survey & Environment, 27(1), 25–28 (in Chinese).

Lin, W.W., and Peng, L.J. (1994) The estimation of Fe^{3+} and Fe^{2+} contents in amphibole and biotite from EPMA data. Journal of Changchun University of Earth Sciences, 24, 155–162 (in Chinese with English abstract).

Linnen, R.L. (1998) The solubility of Nb-Ta-Zr-Hf-W in granitic melts with Li and Li+F: constrains for mineralization in rare metal granites and pegmatites. Economic Geology, 93, 1013–1025.

Linnen, R.L., and Cuney, M. (2005) Granite-related rare-element deposits and experimental constraints on Ta-Nb-W-Sn-Zr-Hf mineralization. In: Linnen, R.L., Samson, I.M. (Eds.), Rare Element Geochemistry and Mineral Deposits. Geological Association of Canada Short Course Notes, 17, 45–68.

Linnen, R.L., and Keppler, H. (1997) Columbite solubility in granitic melts: consequences for the enrichment and fractionation of Nb and Ta in the Earth's crust. Contributions to Mineralogy and Petrology, 128, 213–227.

Linnen, R.L., and Keppler, H. (2002) Melt composition control of Zr-Hf fractionation in magmatic processes. Geochimica et Cosmochimica Acta, 66, 3293–3301.

Liu, Y.S., Hu, Z.C., Gao, S., Gunther, D., Xu, J., Gao, C.G., and Chen, H.H. (2008) In situ analysis of major and trace elements of anhydrous minerals by LA-ICP-MS without applying an internal standard. Chemical Geology, 257, 34–43.

Manning, D.A.C., and Henderson, P. (1984) The behaviour of tungsten in granitic melt-vapour systems. Contributions to Mineralogy and Petrology, 86, 286–293.

Mao, J.W., Chen, M.H., Yuan, S.D., and Guo, C.L. (2011) Geological characteristics of the Qinhang (or Shihang) metallogenic belt in South China and spatial–temporal distribution of mineral deposits. Acta Geologica Sinica, 85, 636–658 (in Chinese with English abstract).

Mao, J.W., Cheng, Y.B., Chen, M.H., and Pirajno, F. (2013) Major types and time–space distribution of Mesozoic ore deposits in South China and their geodynamic settings. Mineralium Deposita, 48, 267–294.

Mao, Z.H., Cheng, Y.B., Liu, J.J., Yuan, S.D., Wu, S.H., Xiang, X.K., and Luo, X.H. (2013) Geology and molybdenite Re-Os age of the Dahutang granite-related veinlets-disseminated tungsten ore field in the Jiangxi Province, China. Ore Geology Reviews, 53, 422–433.

Mao, Z.H., Liu, J.J., Mao, J.W., Deng, J., Zhang, F., Meng, X.Y., Xiong, B.K., Xiang, X.K., and Luo, X.H. (2014) Geochronology and geochemistry of granitoids related to the giant Dahutang tungsten deposit, Middle Yangtze River region, China: Implications for petrogenesis, geodynamic setting, and mineralization. Gondwana Research, 7, 1–21.

Monecke, T., Kempe, U., Monecke, J., Sala, M., and Wolf, D. (2002) Tetrad effect in rare earth element distribution patterns: A method of quantification with application to rock and mineral samples from granite-related rare metal deposits. Geochimica et Cosmochimica Acta, 66, 1185–1196.

Monecke, T., Dulski, P., Kempe, U. (2007) Origin of convex tetrads in rare earth element patterns of hydrothermally altered siliceous igneous rocks from the Zinnwald Sn-W deposit, Germany. Geochimica et Cosmochimica Acta 71, 335–353.

Monecke, T., Kempe, U., Trinkler, M., Thomas, R., Dulski, P., and Wagner, T. (2011) Unusual rare earth element fractionation in a tin-bearing magmatic-hydrothermal system. Geology, 39, 295–298.

Monier, G, and Robert, J.L. (1986) Evolution of the miscibility gap between muscovite and biotite solid solutions with increasing lithium content: an experimental study in the system K_2O-Li_2O-MgO-FeO-Al_2O_3-SiO_2-H_2O-HF at 600ºC, 2 kbar P_{H2O}: comparison with natural lithium micas. Mineralogical Magazine, 50, 641–651.

Mysen, B.O. (1990) Relationships between silicate melt structure and petrologic processes. Earth-Science Reviews, 27, 281–365.

Nash, W.P., and Crecraft, H.R. (1985) Partition coefficients for trace elements in silicic magmas. Geochimica et Cosmochimica Acta, 49, 2309–2322.

Neiva, A.M.R. (1987) Geochemistry of white micas from Portuguese tin and tungsten deposits. Chemical Geology, 63, 299–317.

Peretyazhko, I.S., and Savina, E.A. (2010) Tetrad effects in the rare earth element patterns of granitoid rocks as an indicator of fluoride–silicate liquid immiscibility in magmatic systems. Petrology, 18, 514–543.

Pollard, P.J., Pichavant, M., and Charoy, B. (1987) Contrasting evolution of fluorine- and boron-rich tin systems. Mineralium Deposita, 22, 315–321.

Roda, E., Keller, P., Pesquera, A., and Fontan, F. (2007) Micas of the muscovite–lepidolite series from Karibib pegmatites, Namibia. Mineralogical Magazine, 71, 41–62.

Rudnick, R.L., and Gao, S. (2003) Composition of the continental crust. Treatise on Geochemistry, 3, 1–64.

Shannon, R.D. (1976) Revised effective ionic radii and systematic studies of interatomic distances in halides and chalcogenides. Acta Crystallographica, A32, 751–767.

Simons, B., Andersen, J.C.O., Shail, R.K., and Jenner, F.E. (2017) Fractionation of Li, Be, Ga, Nb, Ta, In, Sn, Sb, W and Bi in the peraluminous Early Permian Variscan granites of the Cornubian Batholith: Precursor processes to magmatic-hydrothermal mineralization. Lithos, 278, 491–512.

Song, G.X., Qin, K.Z., Li, G.M., Liu, T.B., Li, J.X., Li, X.H., and Chang, Z.S. (2012) Geochronologic and isotope geochemical constraints on magmatism and associated W-Mo mineralization of the Jitoushan W-Mo deposit, Middle-Lower Yangtze Valley. International Geology Review, 54, 1532–1547.

Song, G.X., Qin, K.Z., Li, G.M., Evans, N.J., and Chen, L. (2014) Scheelite elemental and isotopic signatures: Implications for the genesis of skarn-type W-Mo deposits in the Chizhou Area, Anhui Province, Eastern China. American Mineralogist, 99, 303–317.

Song, S.W., Mao, J.W., Xie, G.Q., Yao, Z.Y., Chen, G.H., Rao, J.F., and Ouyang, Y.P. (2018) The formation of the world-class Zhuxi scheelite skarn deposit: Implications from the petrogenesis of scheelite-bearing anorthosite. Lithos, 312, 153–170.

Song, W.L., Yao, J.M., Chen, H.Y., Sun, W.D., Ding, J.Y., Xiang, X.K., Zuo, Q.S., Lai, C.K. (2018a) Mineral paragenesis, fluid inclusions, H–O isotopes and ore-forming processes of the giant Dahutang W–Cu–Mo deposit, South China. Ore Geology Reviews, 99, 116–150.

Song, W.L., Yao, J.M., Chen, H.Y., Sun, W.D., Lai, C.K., Xiang, X.K., Luo, X.H., and Jourdan, F. (2018b) A 20 m.y. long-lived successive mineralization in the giant Dahutang W–Cu–Mo deposit, South China. Ore Geology Reviews, 95, 401–407.

Stepanov, A.S., Mavrogenes, J.A., Meffre, S., and Davidson, P. (2014) The key role of mica during igneous concentration of tantalum. Contributions to Mineralogy and Petrology, 167, 1009–.

Sun, K.K., and Chen, B. (2017) Trace elements and Sr-Nd isotopes of scheelite: Implications for the W-Cu-Mo polymetallic mineralization of the Shimensi deposit, South China. American Mineralogist, 102, 1114–1128.

Taylor, S.R., and McLennan, S.M. (1985) The Continental Crust: Its Composition and Evolution. Blackwell, Oxford.

Tischendorf, G., Gottesmann, B., Foerster, H.J., and Trumbull, R.B. (1997) On Li-bearing micas: estimating Li from electron microprobe analyses and an improved diagram for graphical representation. Mineralogical Magazine, 61, 809–834.

Tischendorf, G., Foerster, H.J., and Gottesmann, B. (1999) The correlation between lithium and magnesium in trioctahedral micas: improved equations for Li_2O estimation from MgO data. Mineralogical Magazine, 63, 57–74.

Tindle, A.G., and Webb, P.C. (1990) Estimation of lithium contents in trioctahedral micas using microprobe data: application to micas from granitic rocks. European Journal of Mineralogy, 2, 595–610.

Van Lichtervelde, M., Grégoire, M., Linnen, R.L., Béziat, D., and Salvi, S. (2008) Trace element geochemistry by laser ablation ICP-MS of micas associated with Ta mineralization in the Tanco pegmatite, Manitoba, Canada. Contributions to Mineralogy and Petrology, 155, 791–806.

Vernon, R.H., Etheridge, M.A., and Wall, V.J. (1988) Shape and microstructure of microgranitoid enclaves: indicators of magma mingling and flow. Lithos, 22, 1–11.

Wang, H., Feng, C.Y., Li, D.X., Xiang, X.K., and Zhou, J.H. (2015) Sources of granitoids and ore-forming materials of Dahutang tungsten deposit in northern

Jiangxi Province: Constraints from mineralogy and isotopic tracing. Acta Petrologica Sinica, 31, 725–739 (in Chinese with English abstract).

Wang, R.C., Hu, H., Zhang, A.C., Huang, X.L., and Ni, P. (2004) Pollucite and the cesium-dominant analogue of polylithionite as expressions of extreme Cs enrichment in the Yichun topaz–lepidolite granite, southern China. Canadian Mineralogist, 42, 883–896.

Wang, X., Ren, M.H., and Chen, J. (2017) The muscovite granites: Parental rocks to the Nanling Range tungsten mineralization in South China. Ore Geology Reviews, 88, 702–717.

Webster, J.D., Holloway, J.R., and Hervig, R.L. (1989) Partitioning of lithophile trace elements between H_2O and H_2O + CO_2 fluids and topaz rhyolite melt. Economic Geology, 84, 116–134.

Wood, S.A., and Samson, I.M. (2000) The hydrothermal geochemistry of tungsten in granitoid environments: I. Relative solubilities of ferberite and scheelite as a function of T, P, pH, and m_{NaCl}. Economic Geology, 95, 143–182.

Wu, C.Z., Liu, S.H., Gu, L.X., Zhang, Z.Z., Lei, R.X. (2011) Formation mechanism of the lanthanide tetrad effect for a topaz- and amazonite-bearing leucogranite pluton in eastern Xinjiang, NW China. Journal of Asian Earth Sciences, 42, 903–916.

Wu, F.Y., Liu, X.C., Ji, W.Q., Wang, J.M., and Yang, L. (2017) Highly fractionated granites: Recognition and research. Science China-Earth Sciences, 60, 1201–1219.

Yin, L, Pollard, P.J., Hu, S.X., and Taylor, R.G. (1995) Geologic and geochemical characteristics of the Yichun Ta-Nb-Li deposit, Jiangxi Province, South China. Economic Geology, 90, 577–585.

Yin, R., Wang, R.C., Zhang, A.C., Hu, H., Zhu, J.C., Rao, C., and Zhang, H. (2013) Extreme fractionation from zircon to hafnon in the Koktokay No. 1 granitic pegmatite, Altai, northwestern China. American Mineralogist, 98, 1714–1724.

Zajacz, Z., Halter, W.E., Pettke, T., and Guillong, M. (2008) Determination of fluid/melt partition coefficients by LA-ICPMS analysis of co-existing fluid and silicate melt inclusions: Controls on element partitioning. Geochimica et Cosmochimica Acta, 72, 2169–2197.

Zhang, Q., Zhang, R.Q., Gao, J.F., Lu, J.J., and Wu, J.W. (2018) In-situ LA-ICP-MS trace element analyses of scheelite and wolframite: Constraints on the genesis of veinlet-disseminated and vein-type tungsten deposits, South China. Ore Geology Reviews, 99, 166–179.

Zhang, Y., Yang, J.H., Chen, J.Y., Wang, H., Xiang, Y.X. (2017) Petrogenesis of Jurassic tungsten-bearing granites in the Nanling Range, South China: Evidence from whole-rock geochemistry and zircon U–Pb and Hf–O isotopes. Lithos, 278–281, 166–180.

Zhao, J.H., Zhou, M.F., Yan, D.P., Zheng, J.P., and Li, J.W. (2011) Reappraisal of the ages of Neoproterozoic strata in South China: no connection with the Grenvillian orogeny. Geology, 39, 299–302.

Zhao, W.W., Zhou, M.F., Li, Y.H.M., Zhao, Z., and Gao, J.F. (2017) Genetic types, mineralization styles, and geodynamic settings of Mesozoic tungsten deposits in South China. Journal of Asian Earth Sciences, 137, 109–140.

Zhao, Z.H., Masuda, A., Shabani, M.B. (1992) Tetrad effects of rare-earth elements in rare-mental granites. Geochimica, 3, 221–233 (in Chinese with English abstract).

DOI: https://doi.org/10.2138/am-2019-6796

FIGURE CAPTIONS

FIGURE 1. **(a)** Distribution of Neoproterozoic granites and Mesozoic granites and volcanic rocks in South China (modified from Li et al. 2010), and locations of the Nanling W–Sn polymetallic region (NLR) and the Dahutang tungsten deposit. **(b)** Geological sketch map of the Dahutang tungsten deposit and surrounding areas in northwestern Jiangxi Province, South China (after Jiangxi Western Geological Brigade). Abbreviation: Jiangshan-Shaoxin fault (JSF).

FIGURE 2. Geological map of the Central and North ore blocks of Dahutang tungsten deposit, and location of drilling Site ZK 15-1 (modified from Northwestern Geological Brigade, Jiangxi Bureau of Geology, Mineral Resources, Exploration and Development, 2012).

FIGURE 3. Petrographic characteristics of granites in the Dalingshang ore block, Central Dahutang tungsten deposit. **(a)** Photomicrograph of biotite granite, mineral inclusions in biotite phenocryst form a dark rim; **(b, c)** back-scattered electron (BSE) images of biotite granite show mineral inclusions (e.g., zircon, rutile, ilmenite, monazite, and apatite) in biotite phenocrysts; **(d)** photomicrograph of biotite granite, fine-grained muscovite surrounding the biotite phenocryst; **(e)** photomicrograph of muscovite granite; **(f)** photomicrograph of Li-mica granite. Mineral abbreviations: biotite (Bt), muscovite (Ms), quartz (Qz), plagioclase (Pl), K-feldspar (Kfs), zircon (Zrn), rutile (Rt), ilmenite (Ilm), monazite (Mnz), apatite (Ap).

FIGURE 4. **(a)** A/NK vs. A/CNK diagram indicating the peraluminous nature of granites from the Dalingshang ore block; Plots of **(b)** Al_2O_3 vs. SiO_2, **(c)** TiO_2 vs. MgO, **(d)** MgO vs. Fe_2O_3 show the variation in the major element composition of the granites from the Dalingshang ore block. The data of two-mica granites from the Shiweidong ore block (Huang and Jiang 2014) were shown for comparison.

FIGURE 5. **(a)** Chondrite-normalized REE patterns and **(b)** mean

upper-crust-normalized multi-element diagrams showing the trace element composition of granites from the Dalingshang ore block. Chondrite and mean upper crust values are from Taylor and McLennan (1985) and Rudnick and Gao (2003), respectively. The shaded area represents the chondrite-normalized REE patterns of two-mica granites from the Shiweidong ore block (Huang and Jiang 2014).

FIGURE 6. BSE images of zoned micas in muscovite granite **(a, b)** and Li-mica granite **(c, d)**. The zoned micas in both granite types consist of core, mantle, and rim domains. The mantle forms the brightest domain and has an irregular diffuse boundary where in contact with darker core domain. The rim shows the darkest contrast and exhibits an irregular boundary and clinkery relict of the mantle and sometimes the porous. Mineral abbreviations: muscovite (Ms), quartz (Qz), plagioclase (Pl), K-feldspar (Kfs). The marked numbers are corresponding to analyses of representative compositions, as provided in Appendix 2.

FIGURE 7. Chemical composition of micas in granites from the Dalingshang ore block, shown on ternary diagrams with the apices Al–R^{2+}–Si **(a)** and Li–R^{2+}–Al **(b)** (see main text for details), $R^{2+} = Fe^{2+} + Mn^{2+} + Mg^{2+}$. These diagrams have been constrained using an experimental calibration (Monier and Robert 1986, Foster 1960). Abbreviations: biotite granite (BTG), muscovite granite (MSG), Li-mica granite (LMG).

FIGURE 8. Plots of **(a)** Rb_2O vs. F, **(b)** Cs vs. K/Rb, **(c)** F vs. K/Rb, and **(d)** Li vs K/Rb for micas in granites from the Dalingshang ore block. Abbreviations: biotite granite (BTG), muscovite granite (MSG), Li-mica granite (LMG).

FIGURE 9. **(a–d)** Plots of MgO, FeO^T, F, and TiO_2 versus K/Rb for micas, and **(e–h)** for whole-rock compositions from granites in the Dalingshang ore block. Abbreviations: biotite granite (BTG), muscovite granite (MSG), Li-mica granite (LMG).

FIGURE 10. **(a–c)** Plots of Nb/Ta, Ta, and W versus K/Rb for micas, and **(d–f)** whole-rock compositions from granites in the Dalingshang ore block. Abbreviations: biotite granite (BTG), muscovite granite (MSG), Li-mica granite (LMG).

FIGURE 11. Traverse EPMA analyses of micas from core to mantle to rim along **(a)** line A–B (muscovite) shown in Fig. 6b, and **(b)** line C–D (Li-mica) shown in Fig. 6d.

FIGURE 12. Plots of Li, F, Rb, Cs, W, Sn, Nb, and Ta versus Nb/Ta for zoned micas in muscovite granite and Li-mica granite. Abbreviations: biotite granite (BTG), muscovite granite (MSG), Li-mica granite (LMG).

FIGURE 13. Schematic representation of the processes of enrichment and migration of tungsten in the Dahutang granite and the formation of the Dahutang tungsten deposit. **(a)** The formation of Dahutang tungsten deposit. The sequence of intrusion is according to the sampling depth and Song et al. (2018a, b). Abbreviations: biotite granite (BTG), muscovite granite (MSG), Li-mica granite (LMG), muscovite (Ms). **(b)** Sketch showing the textural and compositional variations of micas in the muscovite granite. **(c)** Sketch showing the textural and compositional variations of micas in the Li-mica granite.

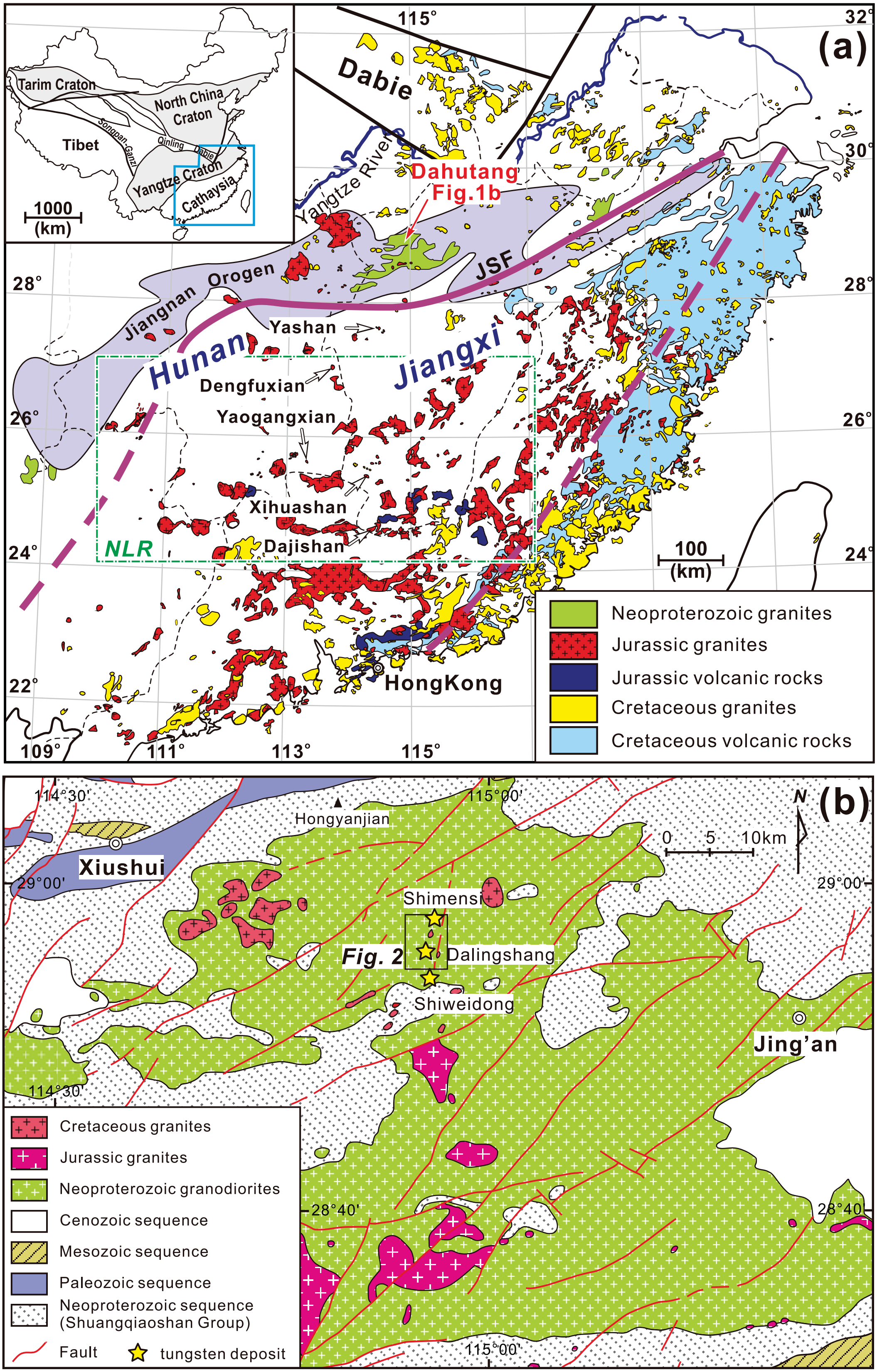

(a)
Tarim Craton
North China Craton
Tibet
Songpan-Ganzi
Qinling
Dabie
Yangtze Craton
Cathaysia
1000 (km)
115°
32°
30°
28°
26°
24°
22°
109°
111°
113°
115°
Dabie
Yangtze River
Dahutang Fig.1b
Jiangnan Orogen
JSF
Hunan
Jiangxi
Yashan
Dengfuxian
Yaogangxian
Xihuashan
Dajishan
NLR
HongKong
100 (km)
Neoproterozoic granites
Jurassic granites
Jurassic volcanic rocks
Cretaceous granites
Cretaceous volcanic rocks
(b)
114°30'
115°00'
29°00'
28°40'
Hongyanjian
Xiushui
N
0 5 10km
Shimensi
Fig. 2
Dalingshang
Shiweidong
Jing'an
Cretaceous granites
Jurassic granites
Neoproterozoic granodiorites
Cenozoic sequence
Mesozoic sequence
Paleozoic sequence
Neoproterozoic sequence (Shuangqiaoshan Group)
Fault
tungsten deposit

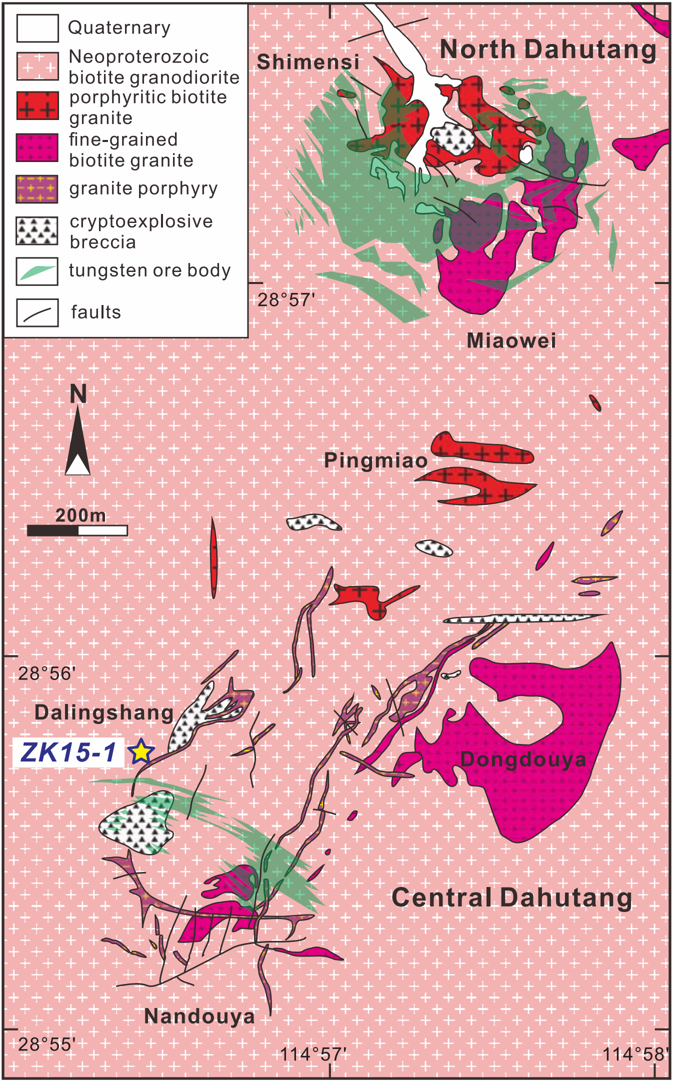
Quaternary
Neoproterozoic biotite granodiorite
porphyritic biotite granite
fine-grained biotite granite
granite porphyry
cryptoexplosive breccia
tungsten ore body
faults
North Dahutang
Shimensi
28°57'
Miaowei
N
Pingmiao
200m
28°56'
Dalingshang
ZK15-1
Dongdouya
Central Dahutang
Nandouya
28°55'
114°57'
114°58'

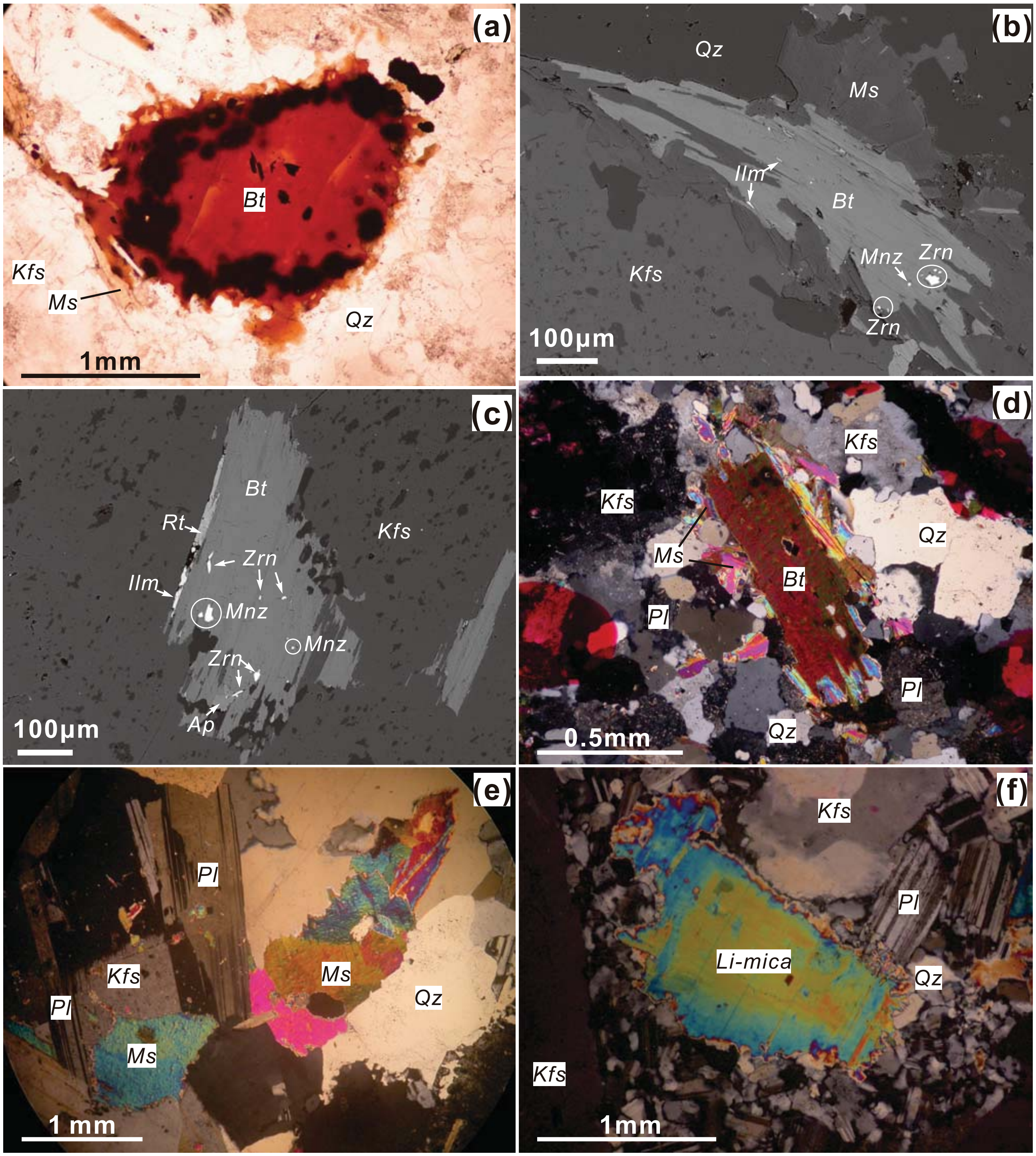
(a)
Bt
Kfs
Ms
Qz
1mm
(b)
Qz
Ms
Ilm
Bt
Kfs
Mnz
Zrn
Zrn
100μm
(c)
Bt
Rt
Kfs
Zrn
Ilm
Mnz
Mnz
Zrn
Ap
100μm
(d)
Kfs
Kfs
Qz
Ms
Bt
Pl
Pl
Qz
0.5mm
(e)
Pl
Kfs
Pl
Ms
Qz
Ms
1 mm
(f)
Kfs
Pl
Li-mica
Qz
Kfs
1mm

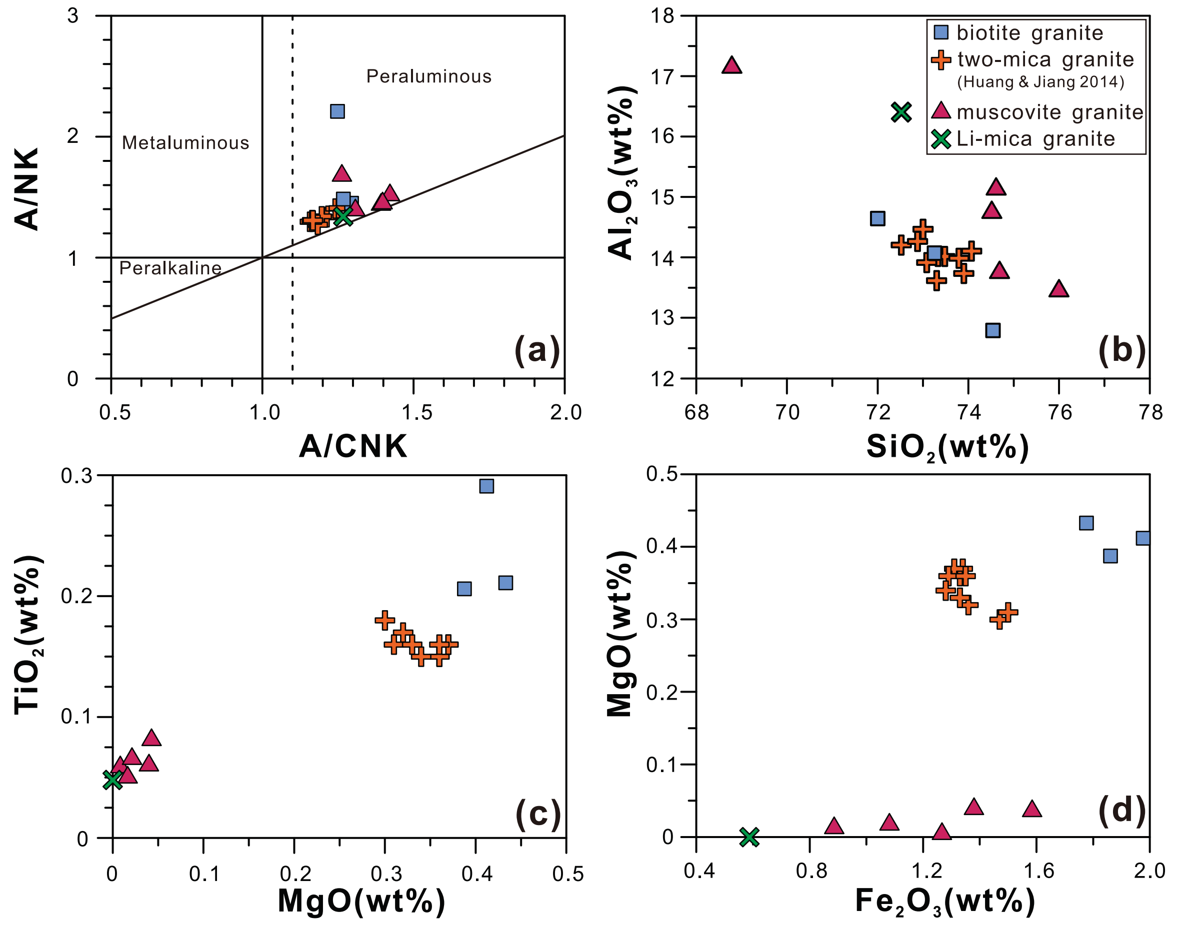

A/NK
A/CNK
Metaluminous
Peraluminous
Peralkaline
(a)
Al_2O_3(wt%)
SiO_2(wt%)
biotite granite
two-mica granite
(Huang & Jiang 2014)
muscovite granite
Li-mica granite
(b)
TiO_2(wt%)
MgO(wt%)
(c)
MgO(wt%)
Fe_2O_3(wt%)
(d)

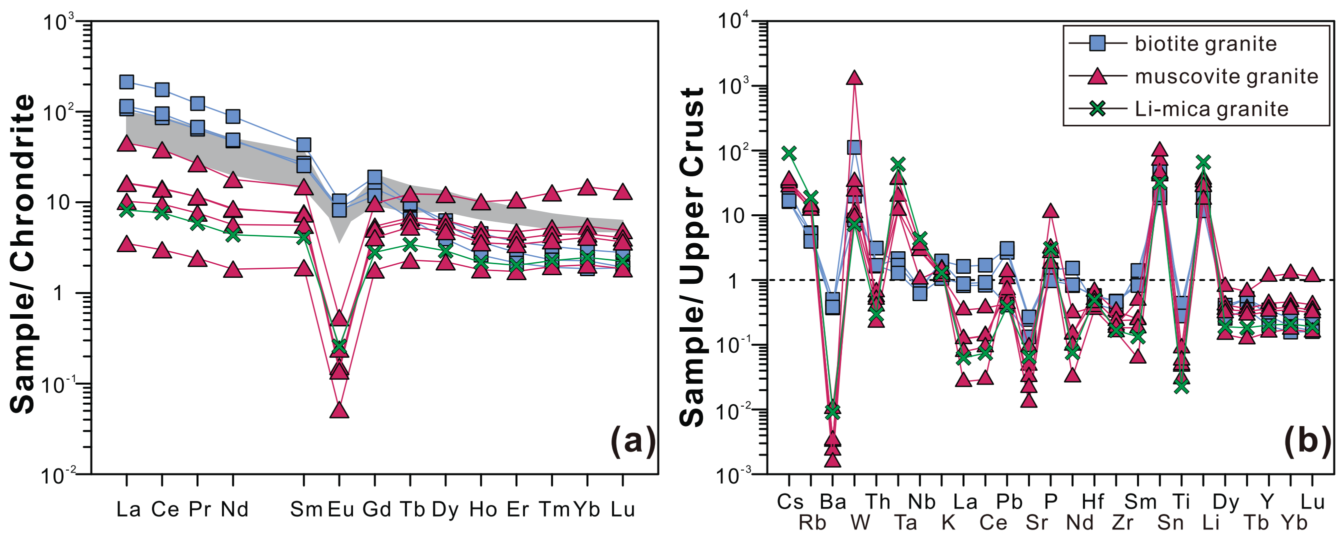

Sample/ Chrondrite
La
Ce
Pr
Nd
Sm
Eu
Gd
Tb
Dy
Ho
Er
Tm
Yb
Lu
(a)
Sample/ Upper Crust
biotite granite
muscovite granite
Li-mica granite
Cs
Rb
Ba
W
Th
Ta
Nb
K
La
Ce
Pb
Sr
P
Nd
Hf
Zr
Sm
Sn
Ti
Li
Dy
Tb
Y
Yb
Lu
(b)

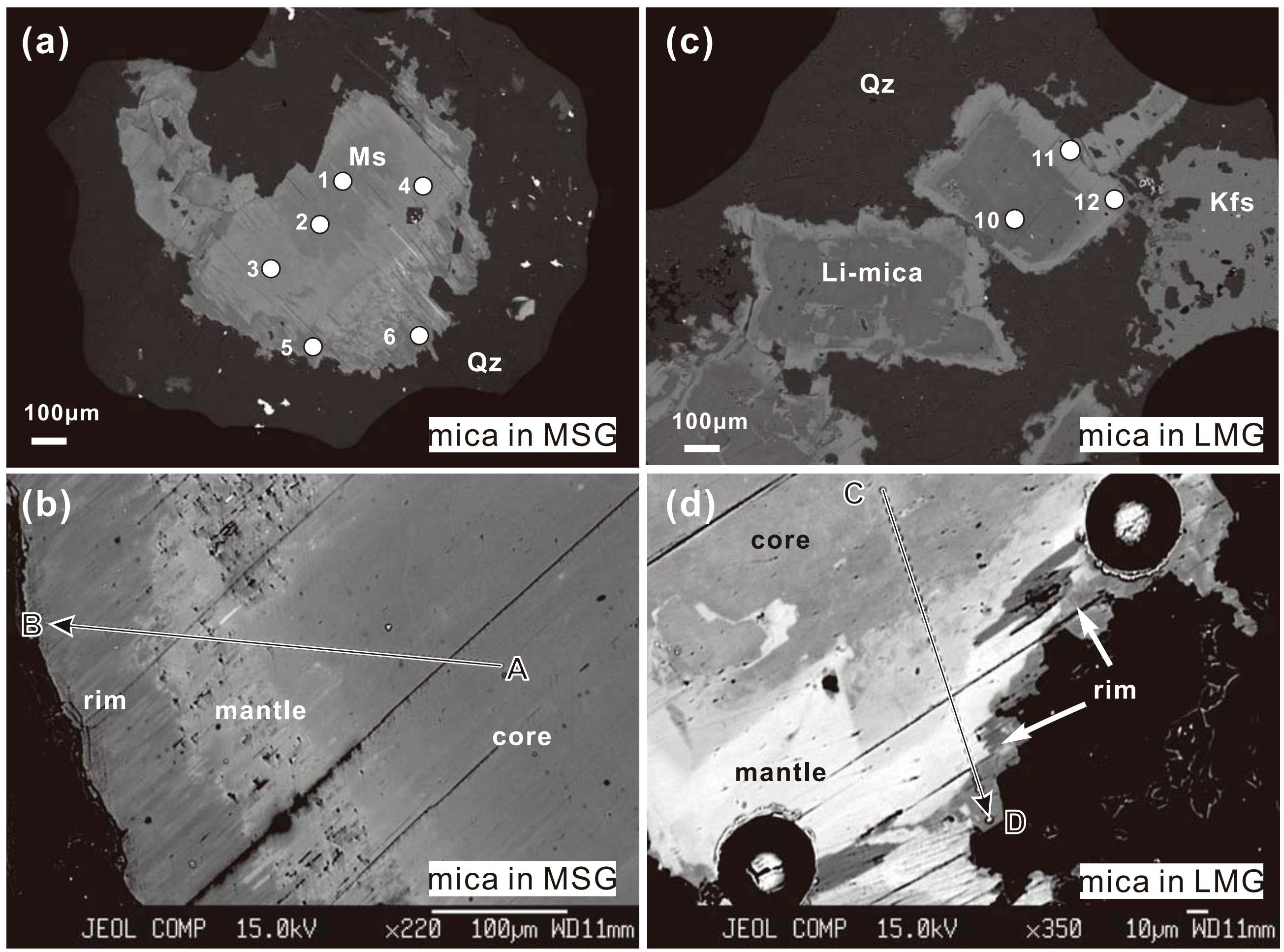

(a)
Ms
1
2
3
4
5
6
Qz
100μm
mica in MSG
(b)
B
A
rim
mantle
core
mica in MSG
JEOL COMP 15.0kV ×220 100μm WD11mm
(c)
Qz
11
10
12
Kfs
Li-mica
100μm
mica in LMG
(d)
C
core
rim
mantle
D
mica in LMG
JEOL COMP 15.0kV ×350 10μm WD11mm

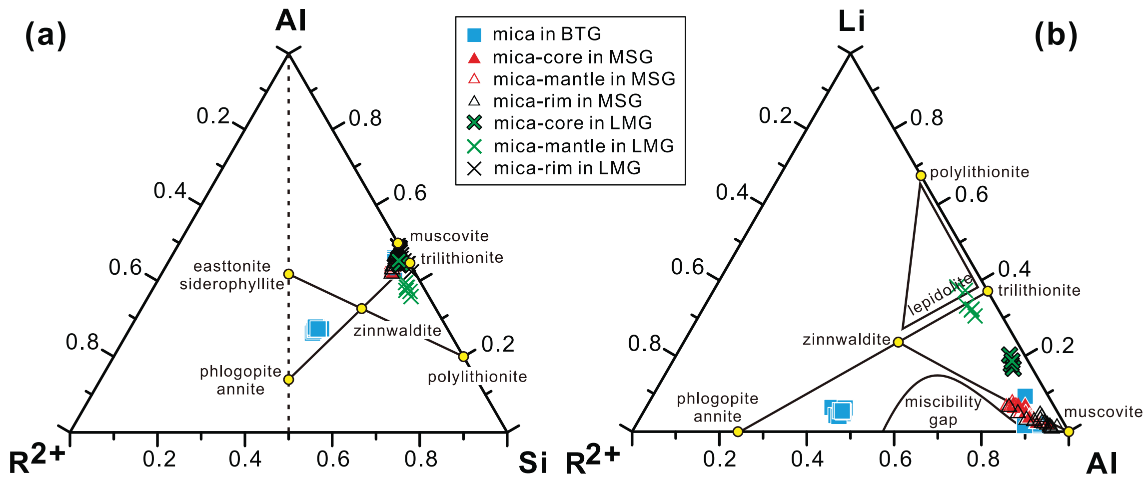

(a)
Al
R2+
Si
0.2
0.4
0.6
0.8
easttonite
siderophyllite
phlogopite
annite
zinnwaldite
muscovite
trilithionite
polylithionite
mica in BTG
mica-core in MSG
mica-mantle in MSG
mica-rim in MSG
mica-core in LMG
mica-mantle in LMG
mica-rim in LMG
(b)
Li
Al
polylithionite
lepidolite
trilithionite
zinnwaldite
miscibility
gap

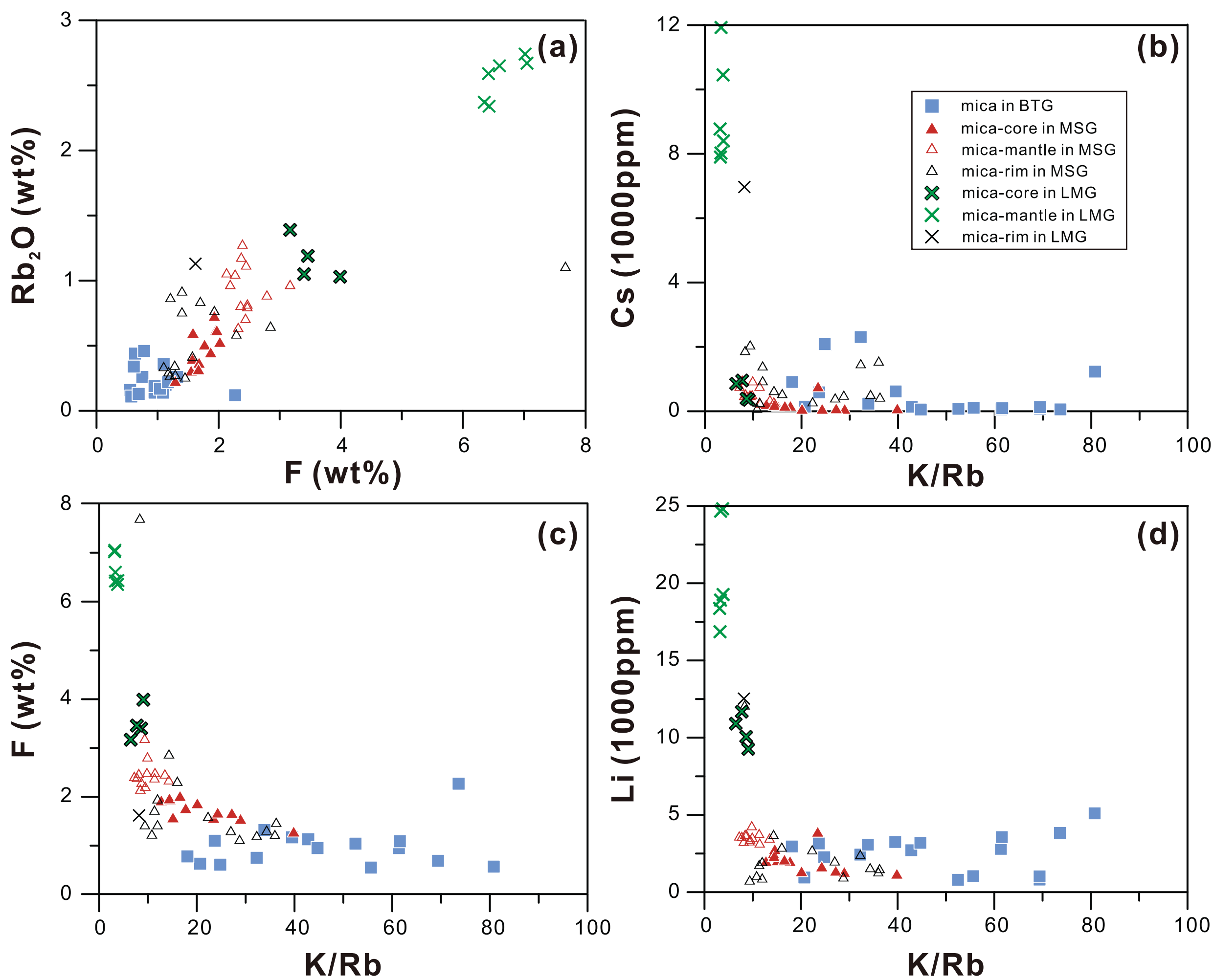

(a)
Rb₂O (wt%)
F (wt%)
(b)
Cs (1000ppm)
K/Rb
mica in BTG
mica-core in MSG
mica-mantle in MSG
mica-rim in MSG
mica-core in LMG
mica-mantle in LMG
mica-rim in LMG
(c)
F (wt%)
K/Rb
(d)
Li (1000ppm)
K/Rb

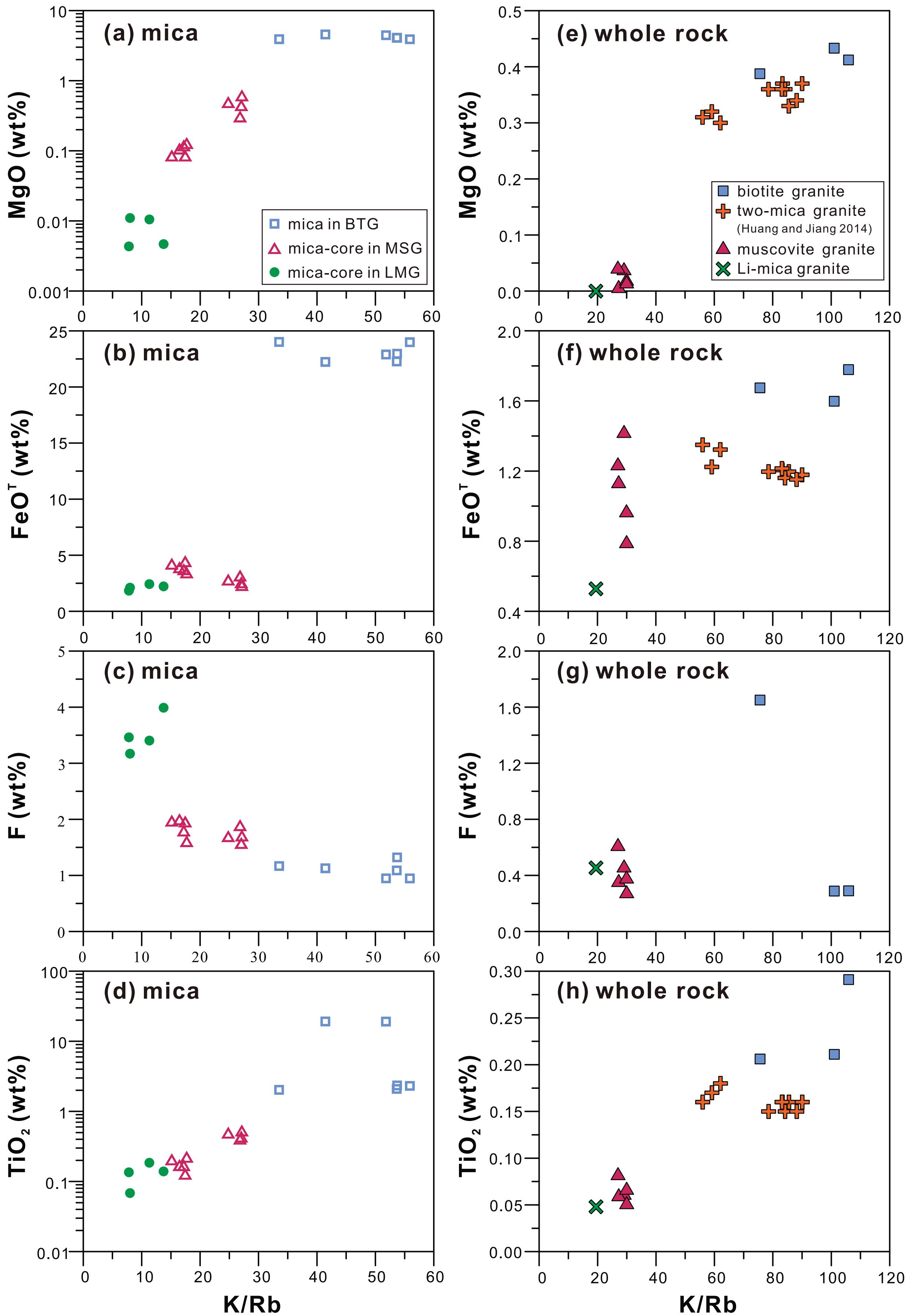
(a) mica
MgO (wt%)
mica in BTG
mica-core in MSG
mica-core in LMG
(b) mica
FeO^T (wt%)
(c) mica
F (wt%)
(d) mica
TiO2 (wt%)
K/Rb
(e) whole rock
biotite granite
two-mica granite
(Huang and Jiang 2014)
muscovite granite
Li-mica granite
(f) whole rock
(g) whole rock
(h) whole rock
K/Rb

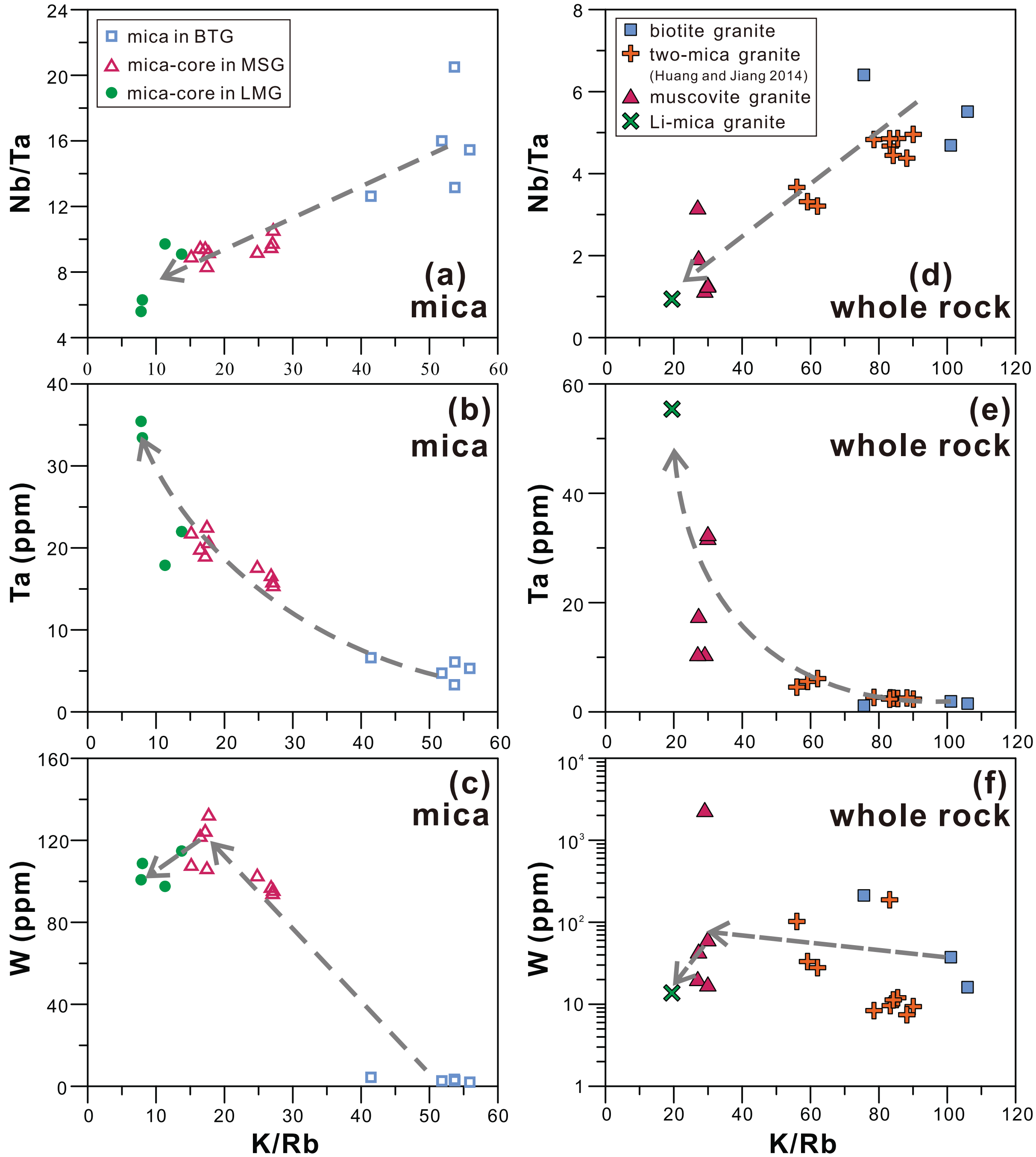
mica in BTG
mica-core in MSG
mica-core in LMG
(a)
mica
(b)
mica
(c)
mica
Nb/Ta
Ta (ppm)
W (ppm)
K/Rb
biotite granite
two-mica granite
(Huang and Jiang 2014)
muscovite granite
Li-mica granite
(d)
whole rock
(e)
whole rock
(f)
whole rock

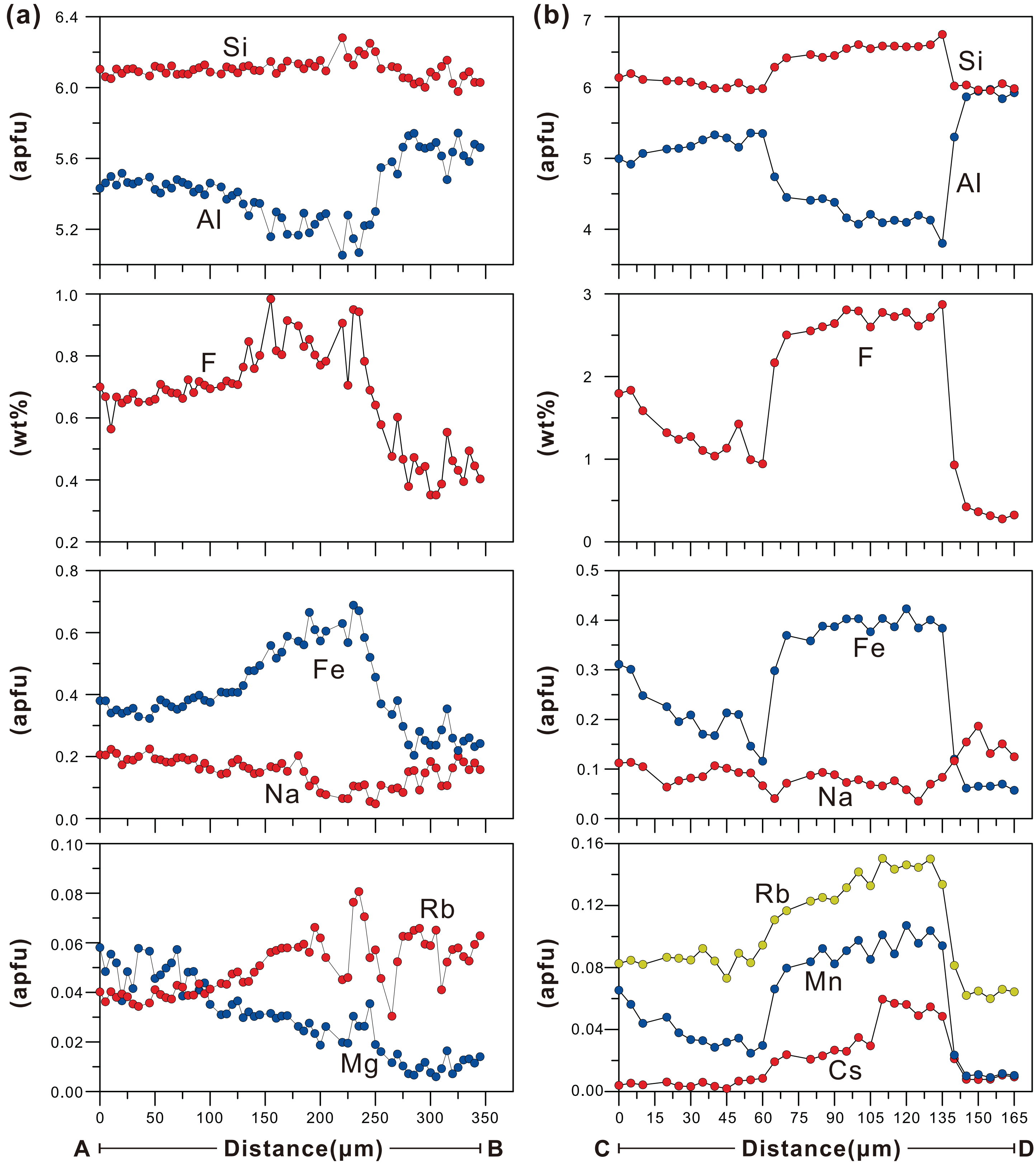
(a)
(b)
Si
Al
F
Fe
Na
Rb
Mg
Mn
Cs
(apfu)
(wt%)
A
Distance(μm)
B
C
D

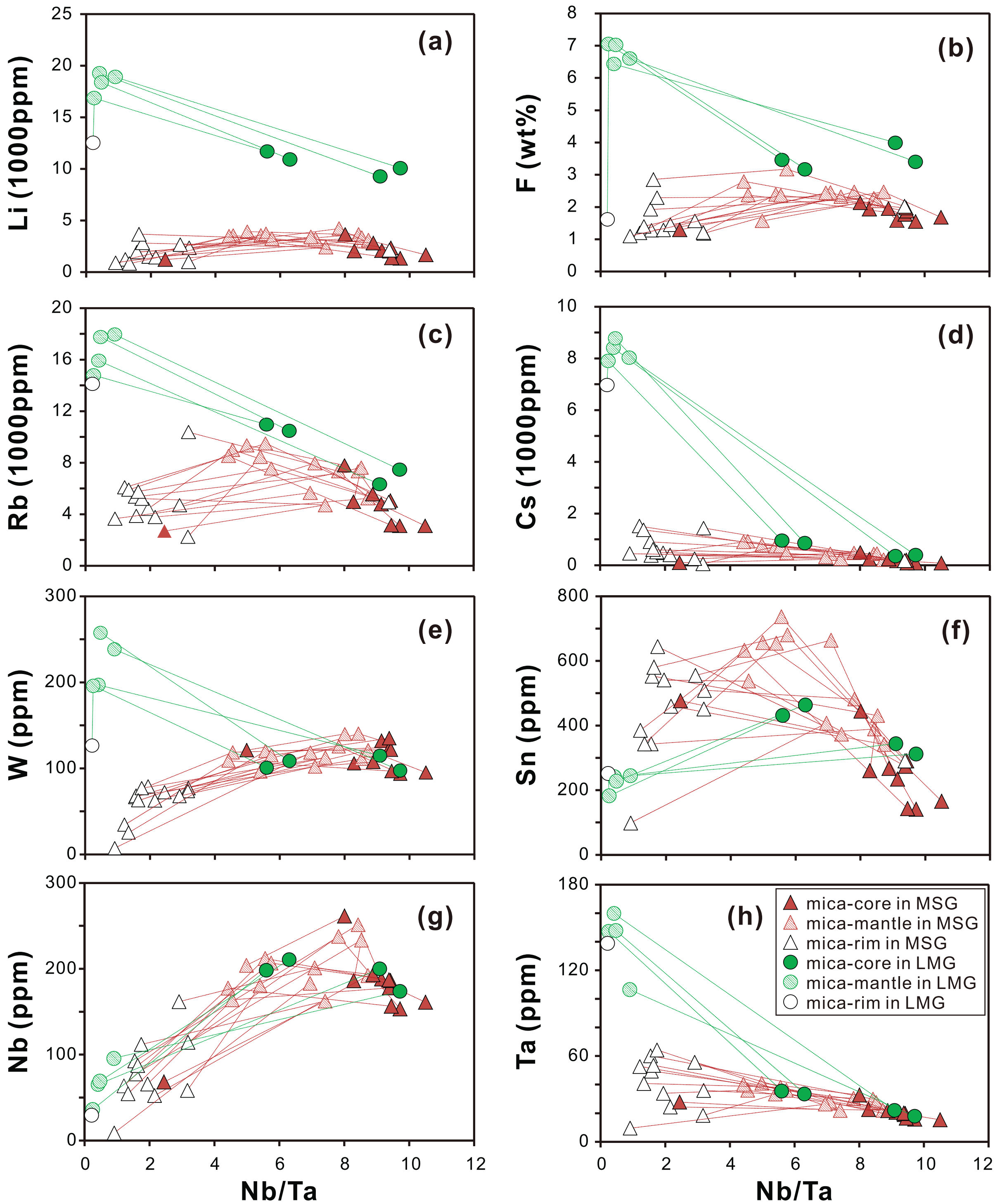

(a)
Li (1000ppm)
(b)
F (wt%)
(c)
Rb (1000ppm)
(d)
Cs (1000ppm)
(e)
W (ppm)
(f)
Sn (ppm)
(g)
Nb (ppm)
(h)
Ta (ppm)
Nb/Ta
mica-core in MSG
mica-mantle in MSG
mica-rim in MSG
mica-core in LMG
mica-mantle in LMG
mica-rim in LMG

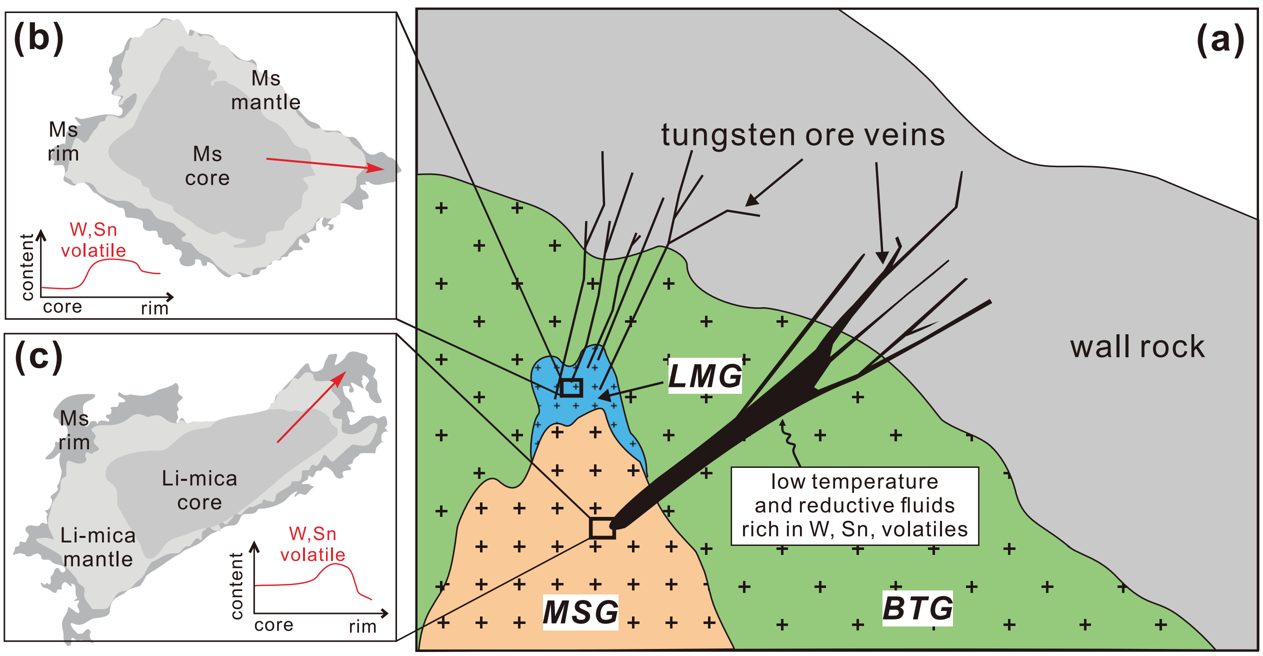

(b)
Ms
mantle
Ms
rim
Ms
core
W,Sn
volatile
content
core
rim
(c)
Ms
rim
Li-mica
core
Li-mica
mantle
W,Sn
volatile
content
core
rim
(a)
tungsten ore veins
wall rock
LMG
low temperature
and reductive fluids
rich in W, Sn, volatiles
MSG
BTG